UNIVERSITY OF VAASA

SCHOOL OF TECHNOLOGY AND INNOVATIONS

COMMUNICATIONS AND SYSTEMS ENGINEERING

Johb Fritz Ekollo

IMPLEMENTATION OF THERMAL AND SPECTRAL IMAGE ANALYSIS FOR NEUROPATHIC FOOT

Master's thesis for the degree of Master of Science in Technology submitted for inspection, in Vaasa June 1st, 2018.

Supervisor Prof. Jarmo Alander

Instructor Dr. Janne Koljonen

FOREWORD

I take this opportunity to express my gratitude to all and sundry for the immense help offered to me in achieving this milestone.

To Professor Mohammed Elmusrati, whom I owe my great gratitude for his ability to listen, willingness, and tremendous support during this study programme. To my supervisor Professor Jarmo Alander, who has been a source of motivation for providing me uninterrupted opportunities, trust and guidance during this thesis. I admit that this thesis would not have achieved its main purpose without the endless assistance of my instructor Dr. Janne Koljonen, for his time and patience. It is also a great pleasure to thank Professor Seppo Hassi, Dr. Vladimir Bochko, Dr. Olli Hautero, Dr. Sofia Svartsjö, Dr. Petri Välisuo and M. Arto Hännonen for all the assistance and support they gave me through this period.

Finally, I would like express my deep grateful to my lovely family, Jayson Dylan Sam, Joyce Sonia Lydi and M.C Anne Lize, for emotional support and constant encouragement, and more explicitly to my mother Lydienne Sissako-Ekollo, for her unquenchable support and undeniable love delineated to me during this moment.

Johb Fritz Ekollo

LIST OF CONTENTS

FOREWORD 2

LIST OF CONTENTS 3

LIST OF SYMBOLS AND ABBREVIATIONS 5

ABSTRACT 7

1 INTRODUCTION 8

1.1 The Objective of this Thesis 9

2 DIABETIC FOOT 12

2.1 Introduction 12

2.2 Neuropathy 13

2.3 Thermal Approach in Diabetic Foot Diagnostics 15

3 THERMAL IMAGING AND IMAGE PROCESSING 17

3.1 Thermal Imaging 17

3.2 Temperature Sensors-Contact/Non-contact 18

3.3 Medical Thermographic Imaging 21

3.4 Image Processing Methods 27

3.4.1 Image Preprocessing 27

3.4.2 Image Segmentation 28

3.4.3 Image Segmentation Parameters for Skin Modeling 28

3.4.3.1 Red Green Blue Colour Space (RGB) 29

3.5 Image Registration 30

3.5.1 Image Fusion Process 30

3.6 Image Analysis based on Thermal and visible images 32

3.7 Camera Calibration for 2-D and 3-D Image Registration 33

3.7.1 Camera Calibration Methods 34

3.7.2 Linear Pin-hole Camera Model 35

3.7.3 Nonlinear Camera Model/Lens Distortion Model 40

4 SPECTRAL IMAGING AND DESIGN 43

4.1 Background and Theory 43

4.2 Diffuse Reflectance Spectroscopy 44

4.2.1 Reflection Spectra Technique 47

4.3 Hyper Spectral Imaging 48

4.3.1 Medical Hyper Spectral Imaging 51

5 EXPERIMENTS AND RESULTS 54

5.1 Overview 54

5.1.1 Equipment 55

5.2 Tests Procedures 57

5.3 Thermal Image Analysis Methods 58

5.4 Spectral Imaging Methods 60

5.5 Registration of Thermal and Spectral Images 62

5.6 Tests and Results 64

6 CONCLUSIONS AND FUTURE WORK 75

REFERENCES 77

LIST OF SYMBOLS AND ABBREVIATIONS

<	Less than
>	More than
$\varepsilon Hb\lambda[Hb]$	Molar Extinction Coefficients of Deoxy-hemoglobin
$\varepsilon HbO_2\lambda$ [HbO_2]	Molar Extinction Coefficients of Oxy-hemoglobin
$\mu_a^{\lambda}, H_2O\lambda$	Optical Absorption Coefficient of Pure water
μ_a^{λ}	Optical Absorption
µm	Micro meter
2-D (3-D)	Two Dimensional (Three Dimensional)
ABI	Ankle-Brachial Index
Arccos	Arc Cosine
Arctan	Arc Tangent
$BaSO_4$	Barium Sulphate Solution
CCD	Charge Coupled Display
COP	Center Of Projection
DCS	Diffuse Correlation Spectroscopy
DLT	Direct Linear Transformation
DNIRS	Diffuse Near-infrared Reflectance Spectroscopy
DRS	Diffuse Reflectance Spectroscopy
FOV	Field Of View
Hb	Deoxy-hemoglobin
$HbA1c$	Glycated Hemoglobin
HbO_2	Oxy-hemoglobin
Hb_{tot}	Total Hemoglobin
Hg	Mercury
HSI	Hue Saturation Intensity
HSI	Hyper Spectral Imaging
IR	Infrared
LCT	Liquid Crystal Thermography

LED	Light-Emitting Diode
LIF	Laser-Induced Fluorescence
log	Logarithm
min	Minimum
MIT	Medical Infrared Thermography
NIR	Near-Infrared
PAD	Peripheral Arterial Disease
PC	Personal computer
PP	Projection Plane
RAC	Radial Alignment Constraint
RGB	Red Green Blue Colour Space
ROI	Region Of Interest
RTD	Resistance Temperature Detector
SAR	Synthetic Aperture Radar
SO_2	Oxygen Saturation
$TcpO_2$	Transcutaneous Oxiometry
UV	Ultraviolet

UNIVERSITY OF VAASA
School of Technology and Innovations
Author: Johb Fritz Ekollo
Topic of the Thesis: Implementation of Thermal and Spectral Image Analysis for Neuropathic Foot
Supervisor: Prof. Jarmo Alander
Instructor: Dr. Janne Koljonen
Degree: Master of Science in Technology
Degree Programme: Communications and Systems Engineering
Major of subject: Communications and Systems Engineering
Minor of subject: Automation Technology
Year of Entering the University: 2014
Year of Completing the Thesis: 2018 **Pages: 85**

ABSTRACT

Diabetes is a grave metabolic disease described by high glucose levels. The feet of patients with diabetes are at the danger of a variety of neurotic results including peripheral vascular infection, disfigurement, ulceration, and necrosis (infection caused by localized death of living cells or tissue) leading to amputation. The way to deal with the diabetic foot is anticipation and early location. Sadly, currently health provider's focus on responsive diabetes mind and the accessibility of lacking subjective demonstrative screening methodology makes doctors miss the finding of a few patients.

The main objective is that diabetic foot demonstrates basic neuropathic and vascular symptoms. When a foot patient is inactive, the thermal recuperation will be much slower. This thermal response speed can be used as a quantitative measure for the study of diabetic foot condition.

In our study, thermal recovery of the foot following cold pressure is discovered using a thermal camera. The captured thermal image is then analysed, and the temperature recovery at each point on the foot is extracted and calibrated using a thermal control appears, and the precarious regions are recognized. In addition, LED-based spectral imaging is tested to estimate oxygen saturation in the foot.

In this subject, we show our examinations on the following parts of the implementation of medical application analytic system based on: measurement protocols, thermal image segmentation, new techniques to perform model analysis of gathered images, and our preliminary discoveries focused on small scale clinical investigation of some patients, which demonstrate the potential of the diagnostic system.

KEYWORDS: Diabetic foot, Thermal imaging, Image analysis, Spectral imaging, Medical application.

1 INTRODUCTION

Diabetes is an important medical issue that is quickly extending. The World Health Organization assessment of 1995 stated that the statistic of diabetic patient around 4% of the world population which is circa 135 million. From various researches, diabetes has been placed as the seventh most common reason of death in the planet. Obviously, the parts of the body most affected by diabetes are the eyes, the kidney and the foot. This thesis focuses on diabetic foot. Different cases about diabetic foot include neuropathy which is a disease or dysfunction of one or more peripheral nerves, that causes partial or total lack of sensation in a part of the body, periphery vein ailments, and tainting will be partly approached in our realised study. From that moment, the lower limb evacuation leads to the foot ulceration which is prevalent to people having diabetes and is placed between 2 to 15 % scale. (Vilcahuaman, 2013)(Reiber & Ledoux, 2003).

Early treatment with medication stops the progression of the diabetic foot. After the complete diagnosis of the diabetic foot, healing footwear, diabetic foot therapy, and typical mind of foot apprehension are used with diabetic medicines. Nevertheless, certified complexities recurrence become to the occasion of an ulcer, may be further reduced by several diabetes evaluation. (Vinik, et al., 2003).

Two essential approaches on which most of the studies concerning diabetic foot are based are:

- Improve the initial diagnosis of diabetic foot in mending focuses.
- Decrease ulcers occasion and related expulsion in diabetic foot.

From all the researches and medical components that can help prevent the damage of the foot, temperature is seen as the basic trademark. Traditional infrared camera has in the past few years increased greatly, with reducing cost and performance improvement. These types of growth are serious contender when showing the different temperature changes in diabetic foot issue. (Mekhontsev, et al., 2010).

For these reasons, evaluating the variations in the temperature of the foot becomes a dynamic point as shown in the forthcoming sections of this thesis. At this stage, the plantar foot temperature observed is normally close to 32 °C. When we examine a control subject, the plantar foot shows temperature variations that are different following values obtained and also shows what is referred to as a corresponding butterfly outline. In fact, the diabetic foot plantar foot temperature changes due to thermoregulation issues which are linked to neuropathy or possibly ischemia and furthermore, if there ought to brings about an event of irritation. (Chan, 1991)(Nagase, 2011).

An article has shown that there is a link between rise in temperature and foot problems in diabetes: before a foot ulcer happens, increased temperature is often seen up to seven days in advance. In diabetic foot, the temperature used to relate the region of interest (ROI) to other parts of the foot is usually as a rule not exceeding a temperature difference of more than 1°C. A temperature rise of more than 2.2°C is not usually seen. The probability of occurrence of foot ulcer can be reduced by a factor of 3 if the increase in temperature between the two feet is recognised and an agreeable treatment is administered. Therefore, one of the approaches shows that ordinary infrared cameras are accurate of contenders due to diagnosis, based on the thermal variation in diabetic foot. (Roback, 2010) (Armstrong, et al., 2006).

1.1 The Objective of this Thesis

Early detectable proof and treatment is the best way to stop diabetic peripheral neuropathy from occurring. Manual examination is the common method for diagnosing periphery neuropathy. These methods are basic and non-invasive and are focused on determining if a patient has lost the sense of feel in the feet. Therefore, if the patients cannot identify the region of a monofilament it is considered that such patient has lost ability to feel and has neuropathy. A huge number of these experiments present basic between irregularity observations. Without doubt, a means for a definite evaluation of preclinical signs of periphery neuropathy which can be repeated would decrease the importance of the fear from this contamination. (Stess, et al., 1986)(Rayman, et al., 1986).

Our method is based on the fact that neuropathy leads to the lack of proper blood circulation in the diabetic foot. Poor thermoregulation is seen in patients affected with neuropathy. In contrast, another theory is made for timely quantitative identifiable proof of diabetic neuropathy due to thermal imaging. Thus, studies have used thermal images to look for skin/tissue temperature variations for patients. The focus will be on the thermoregulation features studied from several measurements taken from the diabetic foot. The reason for this study has been hypothesize by several tests of experiments done to show that with poor thermoregulation, a diabetic foot after being cooled or warmed should recover slower to normal body temperature. (Flynn & Tooke, 1995)(Armstrong, et al., 1997).

In our structure, the past static thermal estimations disadvantage is solved by using a dynamic system. To be more precise, a cool substance like ice is first associated with the diabetic foot, this triggers the thermal auto-course. As the foot warms up to normal body temperature, it is observed with a thermal imaging device. The thermal images taken are put in order and evaluated to give a quantitative measure of the thermoregulation of the foot. The model parameters derived are eventually used to combine the two main points of interests, i.e., diabetic patient with and without risk of periphery neuropathy. It is important to mention that with the presence of high accurate but affordable thermal imaging devices such evaluations are more achievable and possible in the present decade. (Flynn & Tooke, 1995)(Armstrong, et al., 2003).

The main target of the postulation depends on the area of diabetic foot and follows one as of now specified research headings: enhance the early analysis of diabetic foot. It will be founded on the experiments of thermal images of the plantar foot. The conceivable headings are of two namely:

- Find new methodologies to enhance the early conclusion of diabetic foot in health facilities using image analysis.
- Design and test a medical application for dynamic foot temperature experiments using a low-cost thermal camera and LED-based spectral imaging.

The initial step of the task will be to totally comprehend the variations of temperature that are present in diabetic foot before an ulcer occurs. The different postulations are complex factors to enhance this issue. They are most times largely connected to blood dissemination, neuropathic, and infection issues. This process is used to enhance the early analysis of diabetic foot. This thesis is organized in the following way:

In section 1, the meaning of diabetes and its different structures of diabetic foot are given.

In section 2, diabetic foot diseases are introduced. The interest of thermal image processing approach in these cases is illustrated.

The following section 3 describes the utilization of thermal imaging and image processing in different areas, temperature, and especially concentrated on diabetic foot.

From previous analysis, section 4 focuses on diagnosis, spectral imaging and its design to the neuropathic foot.

Section 5 consists of a transversal clinical testing where a few diabetic thermal foot images will be analysed. The analysis shown in this project is multidisciplinary, thermal imaging and image processing, impact factors of body temperature on thermal imaging analysis and applied electronics. Whatever remains of the work is composed as takes after.

Finally, in section 6 detailed conclusions and future work proposals are stated.

2 DIABETIC FOOT

2.1 Introduction

Diabetic foot leading to ulcer is a complex health problem following the different variations of diseases nowadays. The three factors that leads to diabetic foot complexity are ischaemia (other pathological form of diabetes related to restriction in blood vessels and damage or dysfunction of cells and tissues and affecting a given body part, as illustrated in Figure 3), neuropathy, and infection, and they sometimes occur simultaneously. Neuroischaemia is used to describe the occurrence of both neuropathy and ischaemia which occurs most frequently. There have been lengthy evaluations of the peripheral arterial illness in diabetic foot given that diabetics with ischaemia have characteristic ischaemic indications that are regularly reduced than in non-diabetics. (Lepäntalo, et al., 2011).

From the illustration below, vascular blockages occurs in diabetic foot ulcer. In order to ensure the enhancement of diabetic foot ulcer therapeutic and eventually avoid surgical operation, it is important to have an early reference, defensive vascular analysis, imaging and involvement. That means time is a crucial and basic factor to consider when treating the ulcer to keep the foot narrow safe. (Gershater, et al., 2009).

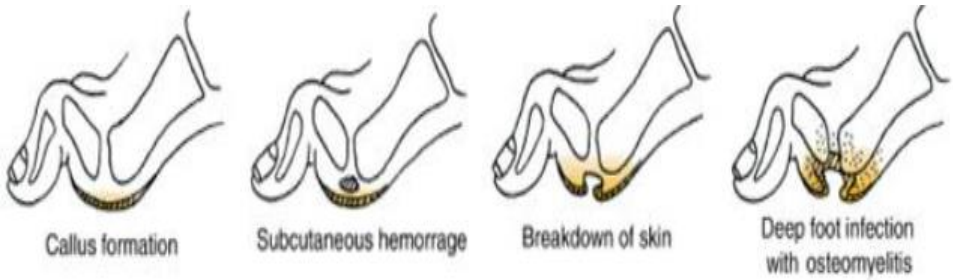

Figure 1. Diabetic wound due to recurrent infection or stress (Bakker, et al., 2011).

A good amount of tissues are damaged when there is delay and poor treatment of diabetes. Diabetic neuropathy is as a result of the damaged nerves in the inferior limbs. This leads to the decrease or total loss of the patient's self-determining and sensory ability.

Exorbitant shear and tension that damages the diabetic foot comes from the loss of defensive sensation, weakened step control, bone deformity (as Charcot foot), callus (bony tissue formed from the healing of a fractured bone) development, and/or blocked sweaty reaction. (Delbridge, et al, 1985). Figures 1 and 2 depict diabetic foot ulcers.

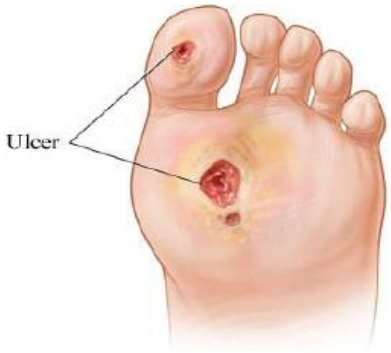

Figure 2. A typical case of foot ulcers (As illustrated in Figure 1).

Poor blood circulation is as a result of the constrictive of the blood vessels to the legs and arms caused by inflammation or damaged tissue. The risk of foot ulcer in diabetic patients is due to iterated trauma to the foot and the guarded defensive or healing reaction as a result of poor vascularization with abnormal formation of blood vessels. Reflectance spectroscopy in the visible room of the electromagnetic spectrum can be used for defensive observation of the damage resulting from diabetes to the feet in diabetic subjects. (Palumbo & Melton, 1995).

2.2 Neuropathy

The three pathological (with chronic and abnormal diseases showing the same initial symptoms) parts that mentions the diabetic foot difficulties are ischaemia, neuropathy, and infection. Most of the time they occur alongside each other as an aetiologic (philosophical study to determine the origin and cause of a disease) threesome. Therefore, the fundamental factors are neuropathy and ischaemia, with various patients showing different weight, and this is as a result of contamination. The lack of defensive sensation of

the foot leads to it being prone to untreated minor wounds resulting from large amount of pressure and thermal damage. (Kalish & Hamdan, 2010).

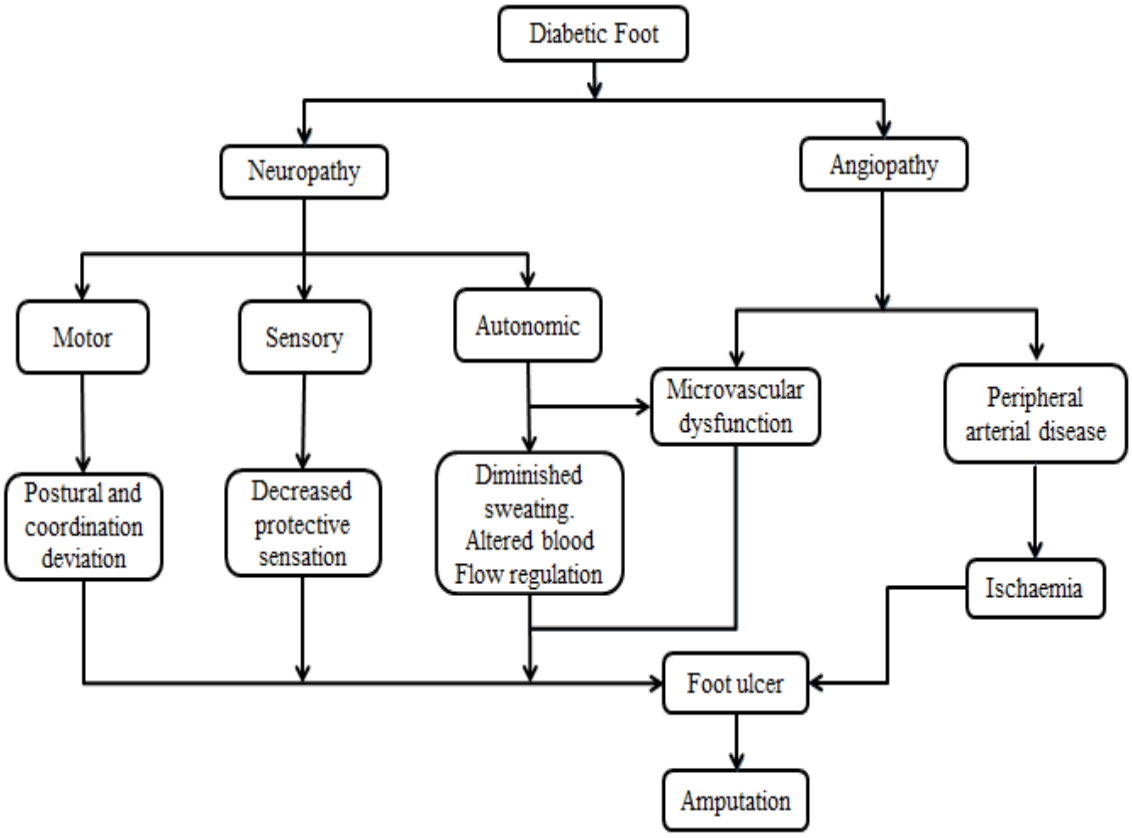

Figure 3. Pathological progression of diabetic foot. (From International Consensus on the Diabetic Foot, 1999).

The foot structures are changed repeatedly by neuropathy which affects the movement of the foot. Hence, this result to the deformity incurs by the foot, coerced articulation abilities and modified stacking of the foot. The important part of the treatment of any ulcer with neuropathy is to restrict weight bearing, without consideration of the closeness of ischaemia. However, the scope of this thesis does not cover the treatment of absolutely neuropathic ulcers. Hence, the term diabetic foot mentioned here defines a diabetic foot ulcer having vascular disability. (Apelqvist, 2008).

2.3 Thermal Approach in Diabetic Foot Diagnostics

Huge expenses and loss of self-esteem are a result of diabetic foot difficulties. Most often, appropriate treatment and a risk analysis of diabetic patients and verification of foot status produced at an early period can lead to the enhancement and deterioration of diabetic foot confusions. Manual examination of foot temperature is the definite healthcare dispense for temperature evaluation. Nevertheless, temperature expansion is mostly too little to be easily identified physically. Therefore, temperature can be a part of the problem solution in this step of diagnosis. (Murff, et al., 1998).

It is a studious process to manually map the foot temperature with a thermometer; therefore, developing a thermographic tool to be used for temperature imaging of the whole foot is in this has been very significance. A two-sided of concept design temperature distribution is done in the plantar foot for a test control patient. Thermoregulations issues distinguish with neuropathy, ischemia, or contamination make the plantar foot temperature to be different in diabetic foot. When compared to an ordinary person, no characteristic form is seen, however, it is possible to detect various shapes. The conceivable changes of the plantar foot temperature are generally below 4 °C in the controls and diabetic foot cases. (Chan, et al., 1991).

The different plantar foot temperature linked to neuropathy was evaluated in a work done by Nagase et al. (2011). He stated that in control persons a less extensive variation is attainable than in diabetic patients. A cold pressure examination is another approach to analyse thermoregulation. Therefore, for the early diagnosis of diabetic neuropathy, temperature changes between the beginning and end of the cold pressure has been useful. Studies have shown that increased temperature can be noticed up to seven days ahead of a foot ulcer occurrence.

Patients often feel trauma as a result of neuropathic episode, which shows that augmented temperature can be a functional predictive indication of foot ulcer and hypodermic damage of the feet in this early stage of the disease. With a particular aim to denote 'increased temperature', an ordered allusion to temperature is needed to be used for a cer-

tain hazard order of patients. Ambient temperature and level of patient's physical movements results to the difference in the temperature of the patients' foot. The sample that is normally used is a comparing region on the opposite foot. Therefore, the requirement is that the temperatures of comparing zones of the right and left foot should not be different with more than 1 °C, and a non-uniform temperature is recorded for temperature variations greater than 2.2 °C. (Armstrong, et al., 1997)(Armstrong, et al., 2006).

Furthermore, situations that stimulate variation in foot temperatures, for example, when there is a frequently equally dispersed temperature change between the feet. In choosing foot temperatures in diabetic patients, there is a technique. Few authors have looked at the subject of diabetic foot temperature appraisal where four achievable methods were put forward of which two have now been apprised into business items by various creators: liquid crystal thermography (LCT), temperature sensors combined into an infrared camera. Hence, the LCT provides data from the heat scattered of the tested foot across a coloured foot, which appears to a spectrum of colours based on the initial temperature. Those colours of the image can be verified with temperatures obtained from an achieved sample. (Lavery, et al., 2004)(Bharara, et al., 2006).

The development of new evaluation tools in this way has become an appealing option. Our study is targeted on developing an intelligent, mobile monitoring complex for continuous examination of the patient feet, to easily differentiate pre-indications of ulceration. Predictive indications for ulcer are the irritation and inflammation in the diabetic feet. Studies have shown that one of the important factors for analysing the risk of diabetic foot ulceration is infrared dermal thermography of the bottom of the foot. (Roback, et al, 2009).

3 THERMAL IMAGING AND IMAGE PROCESSING

3.1 Thermal Imaging

Features of thermal imaging are described as: it is non-active, constructive, non-contact and quite a fast procedure. It gives the observed temperature by making estimation of infrared radiation preceded on surface of the skin. Therefore, the following are incorporated in latest thermal imaging systems: thermal camera with thermal detectors attached to it, signal processing part and image acquisition system sustained by a PC or a mobile phone. In the medical field, specifically in diabetic foot detection, the main focus is on thermal imaging provided in different concept applications. For this reason, thermal imaging is used to measure the body radiation transmitted by a tissue of body. (Bagavathiappan, et al., 2009).

All items above absolute zero expel infrared radiation; this implies that this imaging technique needs no source (that is why it can be said to be passive). The radiating energy of human skin (usually between the wavelengths spectrum of 2 to 14 μm) is without doubt dependent on temperature (T), as found in the Stephan-Boltzmann law:

$$E_b = \sigma T^4, \tag{1}$$

where E_b is the total emissive power, σ is the Stefan-Boltzmann constant, and T is the absolute temperature.

The fundamental way of an advanced thermal imaging system involves different detectors in the central plane of a focal point. Glass cannot be used to make the focal point because it retains unequivocally at wavelengths close to 10 μm. Therefore, germanium is often used to make the focal points used as part of thermal imaging systems (Fauci, et al., 2001).

Objects temperatures which are known are used to adjust the locators in order to get a non-quantified approximation of temperature. Systems that are not aligned have weak reliability (±2 °C); therefore, this is essential in longitudinal evaluations or even examinations including numerous pictures around the same time. It is possible to evaluate the radiation transmitted from the surface of the skin by making use of thermal imaging methods. This is because tissue has a high assimilation factor (25-30 cm^{-1} at wavelengths in the range of vicinity of 2.2 and 5 μm). (Jones & Rehg, 1999).

Thermal imaging is used to determine areas of irritation, or other problem resulting to a supply of defective blood to the tissue (for thermal imaging aims which blood intends heat). Therefore, using thermal imaging to examine fringe blood vessel illness relies on the fact that if the sickness is present, the tissue will have a non-uniform blood supply. Making the temperature around to be in equilibrium is a basic procedure since the anomalous tissue can be uniquely small as 1 °C in comparison to the solid tissue. To achieve this, the patient is made to adjust to the room's specific temperature and this is done exactly or more than 15 minutes before the examinations. A similar test was done to evaluate the temperature of ulcerated and non-ulcerated feet of a similar patient, and it showed that the temperatures of the feet with ulcer were the value is 14.66 °C above the feet without ulcer ($p < 0.0001$). (Armstrong, 1997)(Bagavathiappan, et al., 2009).

The next section articulates on the main concept and the exclusive applications of thermal imaging. It appraises and comprises experiences in the light of studying the thermograph.

3.2 Temperature Sensors-Contact/Non-contact

The categories where different temperature steps are applied are contact and non-contact. Contact temperature measurement techniques used in various applications are comprised thermocouple process, resistance temperature detectors (RTDs), and semiconductor device. Therefore, thermocouples are defined as a part of contact temperature sensors, which have a broadly known applied technology and are often made use of in

measuring temperatures during experiments. On the order hand, non-contact measurement techniques do not require touching the flowing substance or item being quantified. However, the inexpediencies of conventional contact temperature measurement procedures is actually surmounted by making new techniques like optical radiation thermometer using a light beam called laser-induced fluorescence (LIF). (Michalski, et al, 1991).

Effective devices for measuring temperature such as cameras can be used for dependable and advanced measurement and comparison of 2-D or 3-D distribution of temperature. The 2-D distribution of temperature from the patients' foot is achieved using thermal imaging which is a propitious technique for non-contact temperature evaluation. Besides, infrared (IR) thermography and a charge coupled device (CCD) camera are recently used in technology for thermal imaging improvements. Nevertheless, infrared (IR) or near-infrared (NIR) is also a common method applied in experiments involving measuring temperature. Consequently, IR thermography shows meaningful deficiencies like low resolution of the sensors and poor image processing adjustments (edge detection and shape). Therefore, a weak spatial resolution is noticed for filtering. This theory is specifically explained in next section 3.3, which based on movement of the higher radiation to smaller wavelengths. (Huang, et al., 2000)(Dreniak & Boreman, 1996).

The significant physical quantity usually needed for measuring the properties of material (physical, chemical and thermal) is temperature. Its measurement provides regulated and control data of the objects' internal energy. This benefit is important in several industrial techniques. However, using IRT (infrared thermography) for measuring temperature gives the infrared radiation emitted by an object and a conversion into a temperature value is done for the detected energy. (Usamentiaga, et al, 2014).

Each pixel acts for a thermal position seen on an image called thermal infrared image. Thus, the thermal camera gets the radiation given out by the target object in parallel and the radiation emitting from different sources (like objects within close proximity and from the atmosphere), as illustrated in Figure 6.

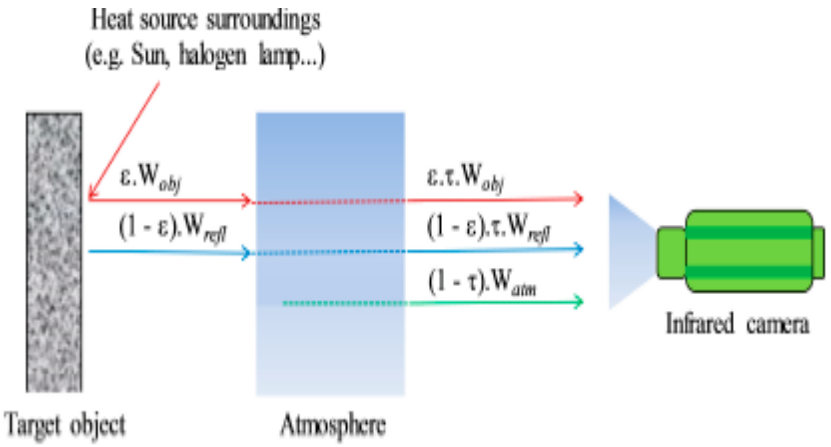

Figure 4. An infrared camera receiving radiation.

Overall, the temperature is obtained according to Figure 4 as follows:

$$\begin{cases} W_{tot} = E_{obj} + E_{refl} + E_{atm}, (a) \\ E_{obj} = \varepsilon_{obj} \cdot \tau_{atm} \cdot \sigma \cdot (T_{obj})^4, (b) \\ E_{refl} = \rho_{obj} \cdot \tau_{atm} \cdot \sigma \cdot (T_{refl})^4 = (1-\varepsilon_{obj}) \cdot \tau_{atm} \cdot \sigma \cdot (T_{refl})^4, (c) \\ E_{atm} = \varepsilon_{atm} \cdot \sigma \cdot (T_{atm})^4 = (1-\tau_{atm}) \cdot \sigma \cdot (T_{atm})^4, (d) \\ W_{tot} = \varepsilon_{obj} \cdot \tau_{atm} \cdot (T_{obj})^4 + (1-\varepsilon_{obj}) \cdot \tau_{atm} \cdot \sigma \cdot (T_{refl})^4 + (1-\tau_{atm}) \cdot \tau \cdot (T_{atm})^4, (e) \\ T_{obj} = \sqrt[4]{\dfrac{w_{tot} - (1-\varepsilon_{obj}) \cdot \tau_{atm} \cdot \sigma \cdot (T_{refl})^4 - (1-\tau_{atm}) \cdot \sigma \cdot (T_{atm})^4}{\varepsilon_{abj} \cdot \tau_{atm} \cdot \sigma}}, (f) \end{cases} \quad (2)$$

where W_{tot} is the total received radiation power to the infrared camera, E_{obj} is emission of the target object, E_{refl} is emission reflected form the object, E_{atm} is emission of the atmosphere, ε_{obj} is emissivity of the object, T_{refl} is the temperature of the object, τ_{atm} is the transmittance of the atmosphere, T_{atm} the atmospheric/ambient temperature, and σ is Stefan-Boltzmann's constant.

Thus, equation (e) is obtained by substituting equations (b) – (d) in (a). However, the temperature of the target object can be computed from (f).

3.3 Medical Thermographic Imaging

In medical point of view, thermal imaging has been applied as a constructive, non-contact, and a technique that can be repeated for measuring and evaluating temperature dispersal of the skin and it is a quick method of providing the temperature map of the body surface of the patient being analysed, without harming the patients. It detects the changes in the temperature on areas of the human skin. Thermal imaging cameras are used to give a high speed and high resolution with significant improvement in stability. The maximal intensity of the human body emission spectrum is related to the wave-length range of 9 μm to 10 μm which is mid-infrared radiation from the microwave range. (Ammer, 2008)(Ring & Ammer, 2000).

$$\begin{cases} P_{net} = P_{emit} + P_{absorb} \\ P_{net} = A\sigma\varepsilon(T^4 - T_0^4) \end{cases}, \tag{3}$$

where P_{net} , P_{emit} and P_{absorb} are respectively the (net, emitted and absorbed) power radiated of the human body, A is the body surface area, (T and T_0) are respectively the body and ambient temperatures, and ε is the emissivity of the surface.

With its emissivity near to the ideal black body, the human skin is referred to as a grey body. Therefore, in the entire spectral range, the emissivity coefficient is uniform and can be summed to the value 0.98. A delicate tissue like the skin has its temperature relying on anatomical and physiological variables. These variables can have an effect on variations of the skin temperature on an area of the human body, therefore, a non-Gaussian thermal distribution is often observed in a specific region of interest (ROI). (Duarte, et al., 2014)(Koprowski, 2015).

The skin’s thermal images are used to give a suitable qualitative visual estimation of temperature spreading. However, quantifiable temperature data is also as important in medical application. Enough details for the estimation of temperature differences and its distribution uniformity are usually not gotten from a single pixel temperature values.

The electromagnetic spectrum has some few medical imaging modalities which are categorised as the scope of radiation frequencies. Information about the physiology of tissues is gotten from Medical Infrared Thermography (MIT) which is fundamentally a digital two-dimensional imaging method. (Merla & Romani, 2005).

MIT is defensive and protective compared to most diagnostic methodologies. What should be addressed is the question of if physiological images can change proceeding to anatomical abruption. Using image fusion in special software, we can combine both morphologies data by restricting the infected area and the level of the damage. The energy from human tissue provides the images, leading to a specimen depending on the energy of light on the human body. Hence, human skin can be seen as a black body radiator with an emissive factor of 0.98 and this implies it is a capable of emitting infrared radiation at body temperature region, in relation to the spectral surface. (Ring & Ammer, 2000)(Steketee, 1973).

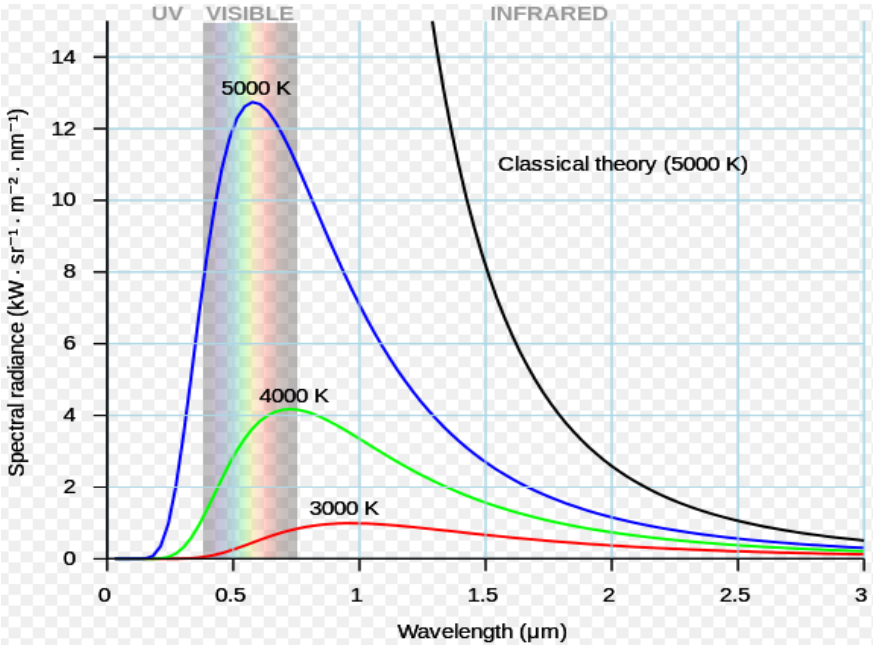

Figure 5. Black body radiation (colored curves) and ultraviolet catastrophe (black curve) described by Planck's law.

Planck’s law reveals in its principles that the emissivity of infrared radiation by a human body is linked in terms of spectral radiant emittance

$$w(\lambda,T)=\frac{2\pi hC^2}{\lambda^4}\left(e^{\frac{hC}{\lambda kT}}-1\right)^{-1}, \tag{4}$$

where h is the Planck's constant, k is the Boltzmann's constant, C is the velocity of light in Vacuum, λ is the wavelength, T is the temperature and $w(\lambda,T)$ is the energy density in a volume of radiation.

Plank's Law approximates that 90% of the infrared radiation emitted from the human body has an extended wavelength spectrum of 8–15 μm. (Figures 6 and 7). Therefore, human skin emits infrared radiation mostly through the visible spectrum of wavelength of 2 - 20 μm range with 9 - 10 μm average peak.

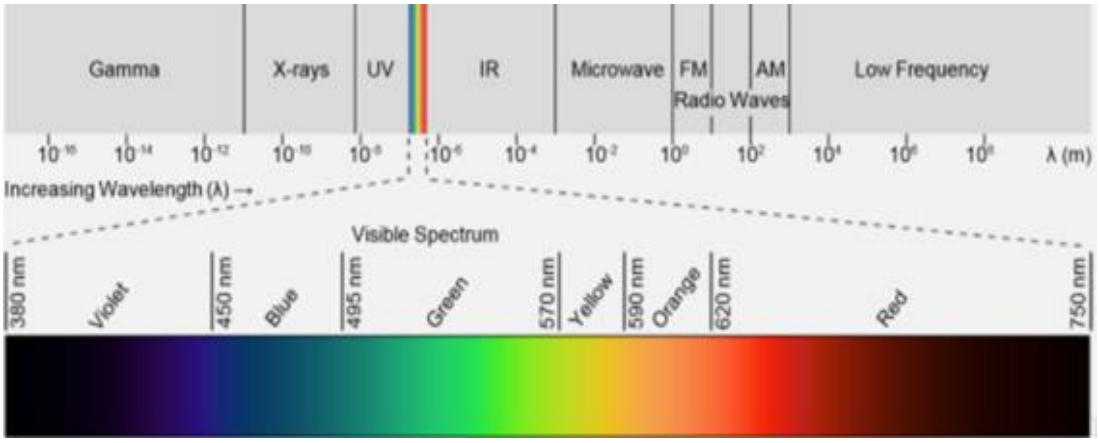

Figure 6. Electromagnetic spectrum with the visible subdivided infrared spectrum.

Emissivity deals with a the ability of a body to give out radiation as seen in the black body emittance principle on which IR thermometry for energy radiated on the surface of an object with its temperature above absolute zero is based. Depending on the amount of energy emitted from the surface by thermal radiation, images can be produced by infrared thermal camera. All incoming radiation for the highest energy achievable at every wavelength of light source is absorbed by a black body (which acts as a radiator). The black body is hence, the fundamental knowledge for the non-contact temperature measurement and for the infrared thermometers calibration. Absorptivity,

transmissivity, and reflectivity are terms used to define the fractions of the total radiant energy linked with each of modes of dissipation. (Steketee, 1973)(Meola, 2012).

$$\begin{cases} \alpha\lambda + \rho\lambda + \tau\lambda = 1 \\ \alpha\lambda = 1 - \rho\lambda \end{cases}, \tag{5}$$

where $\alpha\lambda$ is the spectral absorptance, $\rho\lambda$ is the spectral reflectance, and $\tau\lambda$ is the spectral transmittance.

A blackbody electromagnetic radiation ($W_{\lambda b}$) can be computed from the result of Plank's law (function of λ and T), this is the power emitted for every unit area per unit wavelength.

$$W_{\lambda b} = \frac{W_\lambda}{\varepsilon_\lambda} = \frac{C_1 \lambda^{-5}}{e^{\frac{C_2}{\lambda T}} - 1}, \tag{6}$$

where $W_{\lambda b}$ is the spectral radiant emittance, C_1 and C_2 are the radiation constants, λ is the wavelength and T is the blackbody temperature.

However, the forming of a black body is simple and the concentration of the radiation is not based on angles. At the same temperature, the measure of the ratio of thermal radiation released by a graybody (non-blackbody) compared to a blackbody is referred to as emissivity.

$$L_\lambda = \frac{C_1}{\pi \cdot n^2 . \lambda^2} \cdot (e^{\frac{C_2}{n \cdot \lambda . T}} - 1), \tag{7}$$

where L_λ is the spectral radiance of an isothermal blackbody, C_1 and C_2 are the radiation constants, n is the refractive index of air, λ is the wavelength in air, and T is the thermodynamic temperature.

However, a graybody implies an object having same spectral emissivity at each wavelength and emissivity value of less than 1. In contrast, a non-graybody's emissivity varies in relation to the wavelength. For example, Figure 7 shows the intensity of blackbody radiation increasing at 2 µm with temperature increasing rapidly at 10 µm. This implies that the IR thermometer performs more accurately with greater radiance difference per temperature variation.

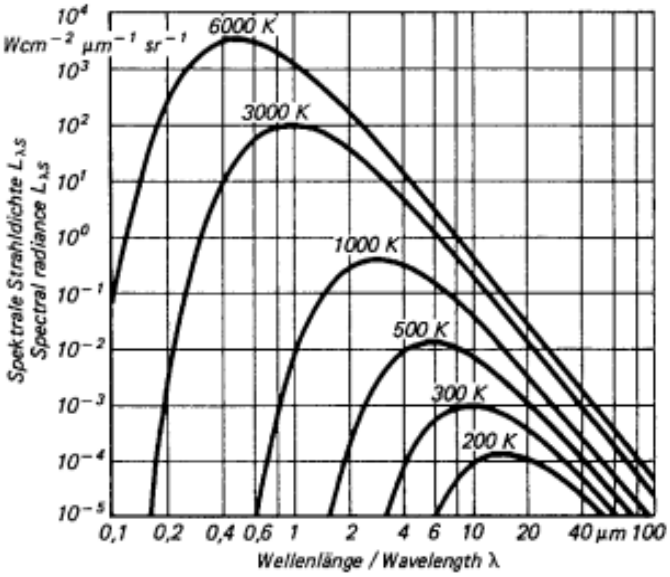

Figure 7. Blackbody radiation in different temperatures. (Richtlinie, 1995).

The wavelength spectrum of a pyrometer which must be chosen according to the temperature range being measured depends on movement of the radiation highest to smaller wavelengths with increasing temperature (Wien's Displacement Law). In temperatures below 600 °C very small radiation energy is observed using an IR thermometer which works fine in lower temperatures at 2 µm. Thus, the drawback of IR thermography has notable improvement using the CCD technique which also gives higher spatial resolution and real-time implementation as the advantages for measuring temperature distribution. (Richtlinie, 1995). (As illustrated in Figure 7).

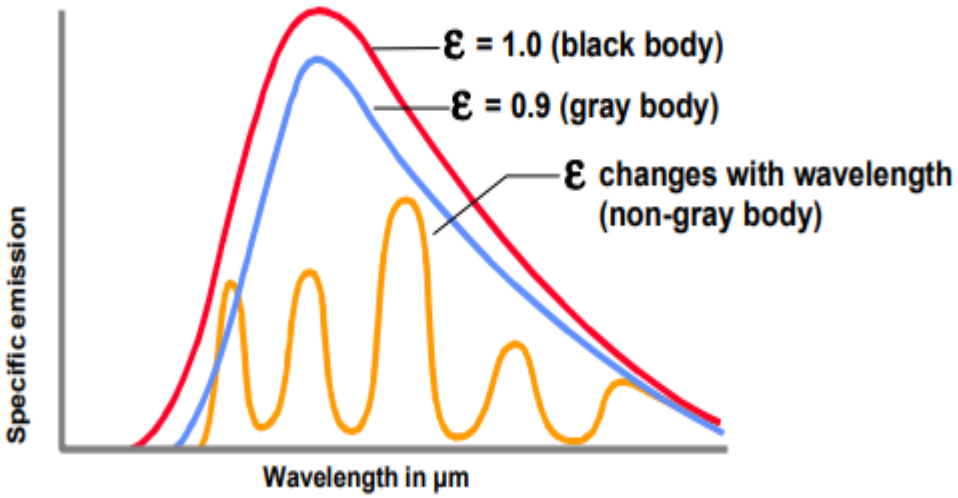

Figure 8. Different types of specific emissions.

The ratio temperature of the surface is computed based on the spectral intensities of the two wavelengths for each pixel given. In the latest research the focus has been on the use of CCD camera for measuring temperature by fixing the IR or near-infrared (NIR) filters right on top of the CCD camera to involve the resolution quality by leading the IR wavelength region and reducing noise. Added to this is an optical amplifier filter set at a definite wavelength to get 2-D monochromatic image. (Huang, et al., 2000) (See Equation 8).

If the emissivity has similar value at both wavelengths, the desired temperature gets is data straight from the device. However, the computation of the spectral energy from two discrete wavelengths is affected by dual-wavelength thermometry. For a FOV that is partly clog up by cold materials like grayscale translucent shows in the sight path, the right temperature of a target can be obtained using this type of device. Hence, the CCD camera produces a temperature which is a result of the brightness at two wavelengths with weak quality images and the choice of filters can improved the quality of the CCD camera when measuring temperature. (Cielo & Vaudreuil, 1992) (Dreniak & Boreman, 1996).

$$\begin{cases} R = \dfrac{L\lambda_1}{L\lambda_2} = \dfrac{\varepsilon\lambda_1 \cdot C_1 \cdot \lambda_1^{-5} \cdot e^{-C_2/\lambda_1 T}}{\varepsilon\lambda_2 \cdot C_1 \cdot \lambda_2^{-5} \cdot e^{-C_2/\lambda_2 T}} \\ = \dfrac{\varepsilon\lambda_1}{\varepsilon\lambda_2} \cdot \left[\dfrac{\lambda_1}{\lambda_2}\right]^{-5} \cdot e^{-\frac{C_2}{T}\left(\frac{1}{\lambda_1}-\frac{1}{\lambda_2}\right)} \\ = \left[\dfrac{\lambda_1}{\lambda_2}\right]^{-5} \cdot e^{-\frac{C_2}{Tr}\left(\frac{1}{\lambda_1}-\frac{1}{\lambda_2}\right)} \\ \dfrac{1}{T} = \dfrac{1}{T_r} + \dfrac{1n\left(\dfrac{\varepsilon\lambda_1}{\varepsilon\lambda_2}\right)}{C_2\left(\dfrac{1}{\lambda_1}-\dfrac{1}{\lambda_2}\right)} \end{cases}, \quad (8)$$

where R is the spectral radiance ratio, C_1 and C_2 are the radiation constants, T is the body temperature, T_r is the ratio temperature of the surface, and $\varepsilon\lambda$ is the spectral emissivity.

3.4 Image Processing Methods

Computer algorithms are used to carry out digital image processing from a source image. Several fundamental steps exist when applying digital image processing to the source image. An image is a two-dimensional function $f(x, y)$, where (x, y) are spatial coordinates and the value of function f at each point (x, y) is respectively proportional to the brightness of the image at each point. (Borgefors, 1984).

3.4.1 Image Preprocessing

In image pre-processing, the data in images are improved prior to further evaluation on the image data. Grayscale conversion and other image amplification techniques are used in the pre-processing procedure to obtain the visual quality required. For example, a Gabor filter is applied to remove the Gabor noise produced by the image acquisition process and to smoothen an image. Therefore, the visual look of an image is done using

scaling resizing which also modifies the quantity of data stored in an image representation. (Gejgus, et al, 2004).

3.4.2 Image Segmentation

In image segmentation context, a digital image is split into different segments, that is, sets of pixels called perfect pixels with the main objective of separating and adjusting the representation of an image into a format that is simpler to examine. Image segmentation is usually applied in locating items and peripheries (e.g. lines, curves) in given images form analysed data source. Evidently, image segmentation involves tagging every pixel of an image in a way that the pixels with a similar performance are labelled the same following some visual features. (Jianbo, et al, 1998).

Skin images segmentation is hard and complex as is some specific colour image segmentation. The changes in texture and colour are a result of the variation in output medical devices. Therefore, executing enough segmentation results rely chiefly on techniques to observe consistency in the typical values of the image points, and then isolating the uniform surface. Image segmentation algorithms are classified into thresholding procedures, edge detection, and region oriented methods. These techniques are used in enhancing various factors that affect the measured intensity value of an object in an image, to involve in finding a notable shift in intensity, and to specify the closed region-oriented in space. (Borgefors, 1984) (Johnston, 1994).

3.4.3 Image Segmentation Parameters for Skin Modeling

The comparison of a known image features such as gray-level value is used by image segmentation algorithms for extracting regions. Several applications cannot use gray-level values alone in the segmentation of images that show various structures or textures. It requires more features details about the structure of the image in order to segment the given images in section 5.6. Thus, images of skin lesions shows significant differences in colour hues and additionally a geometrical aspect of local area structure.

For example, images of epidermic show geometrical structure of pigmentation with a rich combination of skin colour. (Acha, et al, 2005) (Round, et al, 1997).

3.4.3.1 Red Green Blue Colour Space (RGB)

The processing and saving of digital image data usually uses the RGB colour space. However, factors like the high correlation between channels, important perceptive inconsistency combined of chrominance and luminance allows RGB not to be a significantly acceptable choice for colour evaluation and identification algorithms dependent on colour. (Jones & Rehg, 1999).

Therefore, clusters of pixels are made by the image segmentation. Using three-colour vector or RGB triples to compute segmentation takes a huge amount of time and it is intricate since most colour models has three colour channels. Therefore, the scale of colour vectors are decreased by normalized RGB. The RGB values are used for normalization as shown in equation (9):

$$\begin{cases} r = \dfrac{R}{R+G+B} \\ g = \dfrac{G}{R+G+B}, \\ b = \dfrac{B}{R+G+B} \end{cases} \tag{9}$$

where r = Red channel, g = Green channel, and b = Blue channel; respectively for R = Red, G = Green and B = Blue.

For matte surfaces, when ambient light is neglected, the normalized RGB is invariant (under some assumptions) to changes of surface orientation with respect to the light source. This is an exceptional property of this representation. (Tomaz, 2016).

3.5 Image Registration

Image registration is a method of combining the final data from various information sources. This method involves the modification of different sets of data into one coordinate system. Therefore, image registration is applied in the comparison and integration of the data collected from different measurements obtained on various viewpoints and sensors at variations in time. Hence, this technique is used in geometrically aligning two images (source image and sensed image). Harris corner detection method is used to achieve this image registration and also determine the contour features of the target image, but the number of image pixels is so far bigger than the number of corners. (Hui, et al, 2010) (Zhang, et al., 2009).

3.5.1 Image Fusion Process

The technique used to merge two or more images into a single image while keeping the individual significant features of the initial images is referred to as image fusion. This process is often needed for images gotten from several device modalities or capture methods of the similar objects.

The fusion of images finds its application in major areas like medical imaging, microscopic imaging, and computer vision. The basic method of pixel averaging to complex methods like image fusion composition based fusion procedure is part of the general fusion techniques. Image fusion involves the harvesting of valid data from not less than two images. The resultant image will have more data than any of the input images used. (Wang, et al., 2002).

The constraints of applying single sensor data is overcome by using methods such as multi sensor and multi view data processes used in a parametric system. Therefore, extended range of tasks, expanded spatial and temporal resolution, lowered vulnerability; higher precision, reliability and minimal representation are the pros of using image fusion. Hence, a part of the basic fusion technique algorithms also have difficulty and the image is made fuzzier using direct fusion process. Furthermore, for high and accurate

resolution images, the pixel based image combination is relatively complicated using computational algorithm. (Mitchell, 2010).

A decreased contrast of data is produced by the image averaging technique. An original and logical data fusion method is therefore a condition and thus, it is possible to design an effective way and observation system. Some of the data is inessential but also compatible at the same time. Then, the pixel level combination of spatially written input images are recapped in various perspectives based on processes of images analysis. Therefore, the redundant application use band pass filters from each orientation of the source image (rows and columns) followed by a sub step of taking samples which is used in processing the discrete two dimensional transform. (Wang, et al., 2002) (Zhang, et al., 2009).

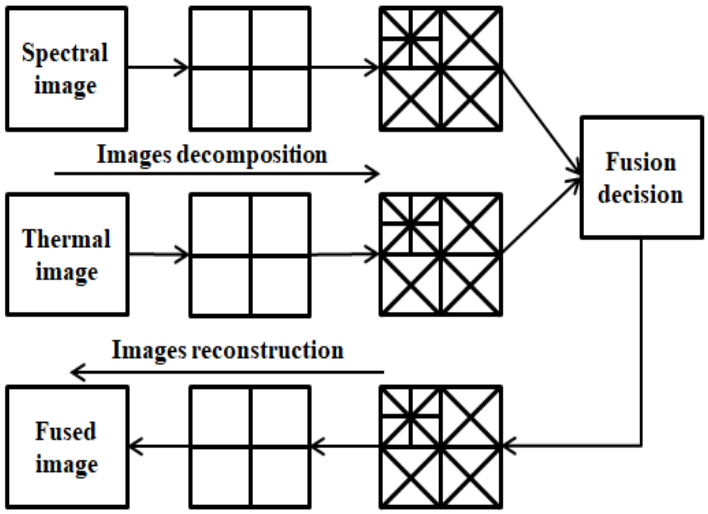

Figure 9. Fusion image analysis.

A scalar fusion transform is used for a single level of decomposition substituting the two-dimensional (2-D) image data with four blocks contrasting to any band pass filtering in each path appearing for the sub-bands. A defined equation over an interval can be represented in terms of an orthonormal function using image fusion analysis which is equivalent to Fourier analysis. Hence, we observe the application of developed theory from thesis experiments in Figure 23.

3.6 Image Analysis based on Thermal and visible images

Image fusion analyses are used widely in different fields. It is usually an important initial preparing part in several computer vision and image analysis function which involves getting imaging data from different sensors, for instance, thermal and visible. An example is human identification involving the recognition of individuals with a fake structure. (Gavrila, 2001).

Combining visible and thermal images is beneficial because visible images are greatly affected by lighting conditions whereas; thermal images give amplified difference between human bodies and their condition. However, it has been noticed that thermal images are reactive to wind and temperature changes in outside conditions. The consolidation of data sources uses probabilistic strategies. (Malviya & Bhirud, 2009).

In general, the term fusion is a process used to deal with detach data obtain in a few spaces. Image fusion is used to achieve the combination of relevant data from a minimum of two images into a single image with the resultant image being more useful than any of the input images. The goal of applying image fusion is to merge the integral multi-sensor, multi-temporal and in addition, multi-view data into one new image containing data, the feature of which cannot be accomplished something different. Detection errors are rescued by the intelligent consolidation of the data from the two sensors. (Bertozzi et al., 2003) (Zhang, et al., 2009).

In previous articles, some of the patients were examined with a couple of them dealing with the feet were discussed. In any case, many papers are available when looking to the attempts in the visible region of the spectrum for identical assignment. In comparison, the idea to couple visible and thermal image is not seen to be an outstanding research field for this application. This is explained most likely as due to the high cost of thermal cameras compared to their visible counterparts. In addition, exterior conditions are obviously highly stimulating to visible imagery due to shadows, light reflections, quantity of darkness, levels of haziness and luminosity. Finally, fusion of thermal and visual im-

age finds it application in enhancing individual detection and fusion execution. (Masoud & Papanikolopoulos, 2003). (Wang, et al., 2002).

Ability for identification under all illumination conditions as well as straight forward anonymity is specified by thermal image which is in comparison immutable to ambient illumination. Remote sensing requests regularly use thermal sensors. The ability to be able to get important data in night or conceivably poor detectable quality conditions is achieved by coupling a thermal sensor with a visual sensor (to save reference or for added spectral data) and precisely processing the two information streams. (Park et al., 2008).

3.7 Camera Calibration for 2-D and 3-D Image Registration

The link between the image coordinate system and space coordinate system is created by camera calibration. The distribution of two dimensional temperatures for the region of interest (ROI) on the surface of a 3D object is created when camera calibration method is combined with temperature measurement methods. This makes camera calibration to be a vital issue to consider in computer vision. Therefore, it is critical for the calibration of the camera to be correct especially for applications such as dimensional measurements and resolution from images which are quantitative calculations. (Huang, et al., 2000).

Recognizing the unknown innate camera model factors is another feature of camera calibration. Measuring the temperature in a pre-stated region of the human body and generating a temperature profile is achieved using camera calibration technology combined with methods used for measuring temperature. Thermal camera and thermocouples are used to generate temperature data and perform various experiments. Using the proposed techniques we generate results that correspond to the data from the thermal camera and thermocouples. (Dreniak & Boreman, 1996) (Renier, et al., 1996).

The temperatures computed from the various experiments revel that these methods produce accurate data which are close in comparison with the thermal gun readings and thermocouples data. In addition, the temperature changes from thermocouples are in line with precise temperature expectations provided by the temperature estimations which are derived from the used methods. (Michalski, et al., 1991).

3.7.1 Camera Calibration Methods

Perspective projection equations, referred to as imaging transformation, shows the relationship of the focal length, field of view, camera position, and angle between cameras to object (As illustrated in Figure 10).

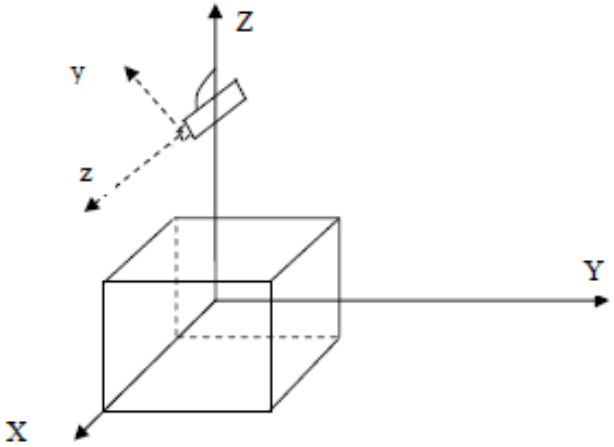

Figure 10. Camera coordinates with respect to the cardboard box coordinates as used in the experiments.

This relation requires a set of image landmarks with their respective space coordinates known. Therefore, camera calibration is the computational process that uses the given points to derive the camera requirements. Therefore, direct linear and nonlinear techniques are the two main classes of the recent methods for camera adjustment. Abel-Aziz and Karara created the Direct Linear Transformation (DLT) in 1971. DLT transforms into linear concept when the lens or focal point distortion is neglected. Tsai's Radial Alignment Constraint (RAC) (1987) camera calibration is a usually used linear algo-

rithm techniques. Hence, comparing accuracy and computation speed it is generally regarded as good choice.

In addition, if the camera sensor plane is parallel to the plane surface stated by the calibration edge this will lead to Tsai's RAC technique to be defeated. On the contrary, a significant number of variables and a large-scale nonlinear optimization are used by nonlinear models which look more exact.

3.7.2 Linear Pin-hole Camera Model

By assuming into consideration a set of k object points which have world space coordinates $\{x_{m,i}, y_{m,i}, z_{m,i}\}$ the calibration of the camera can be done. m denotes the world space coordination, i = 1, …, k that are given with adequate accuracy, and are around the field of view (FOV) of the camera. These points assigned to as adjustment points are monitored on the camera scope at the corresponding image coordinates $\{X_i, Y_i\}$. (Figures 11 and 12).

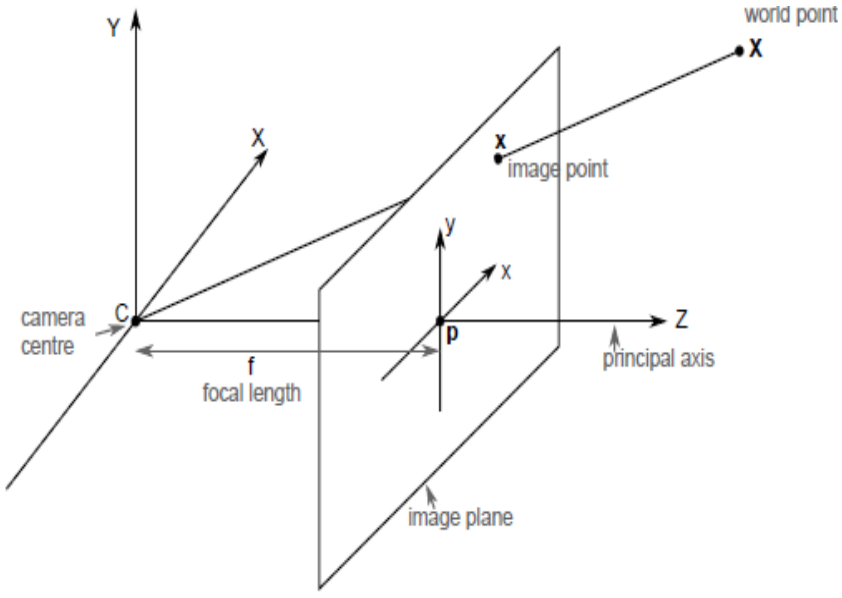

Figure 11. Geometric transform for the pinhole camera model.

where the centre *C* is the camera centre of the projective and *P* is the principal point of the camera. Therefore, the basic camera calibration technique deals with linear least squares identification of the perspective projection transformation matrix.

We use the geometric transform to retrieve the scale and angle of the pinhole camera model. As a result of computing the image transformation from the distorted image to the original image in *C* denoting the camera centre, at this point we have to compute its inverse to recover the distortion by applying matrix transpose of source image.

Let us note the system equations $\begin{cases} \mathrm{sc} = \mathrm{scale} * \cos(\varphi) \\ \mathrm{ss} = \mathrm{scale} * \sin(\varphi) \end{cases}$. Then,

$$(x, y, z) = \begin{pmatrix} sc & -ss & 0 \\ ss & sc & 0 \\ t_x & t_y & 1 \end{pmatrix} = \begin{pmatrix} \psi\cos(\varphi) & -\psi\sin(\varphi) & 0 \\ \psi\sin(\varphi) & \psi\cos(\varphi) & 0 \\ t_x & t_y & 1 \end{pmatrix}, \tag{10}$$

where ψ = scale, t_x and t_y are x and y translations respectively.

The axes of frame x shown from frame y for 2D are generally the columns of the rotation matrix. Thus, coordinate transforms are represented as a single matrix by homogenous coordinates. As previously stated, to obtain arbitrary rotation we combined 3 coordinates.

Therefore, rotations matrix in homogeneous coordinates is denoted in equation (11).

$$\begin{cases} R_x(\varphi) = \begin{bmatrix} 1 & 0 & 0 \\ 0 & \psi\cos(\varphi) & -\psi\sin(\varphi) \\ 0 & \psi\sin(\varphi) & \psi\cos(\varphi) \end{bmatrix} \\ R_y(\theta) = \begin{bmatrix} \psi\cos(\theta) & 0 & -\psi\sin(\theta) \\ 0 & 1 & 0 \\ \psi\sin(\theta) & 0 & \psi\cos(\theta) \end{bmatrix} \\ R_z(\beta) = \begin{bmatrix} \psi\cos(\beta) & -\psi\sin(\beta) & 0 \\ \psi\sin(\beta) & \psi\cos(\varphi) & 0 \\ 0 & 0 & 1 \end{bmatrix} \end{cases}, \tag{11}$$

where $R_x(\varphi)$, $R_y(\theta)$ and $R_z(\beta)$ are rotations matrix in homogeneous coordinates respectively of x, y and z with Euler angles.

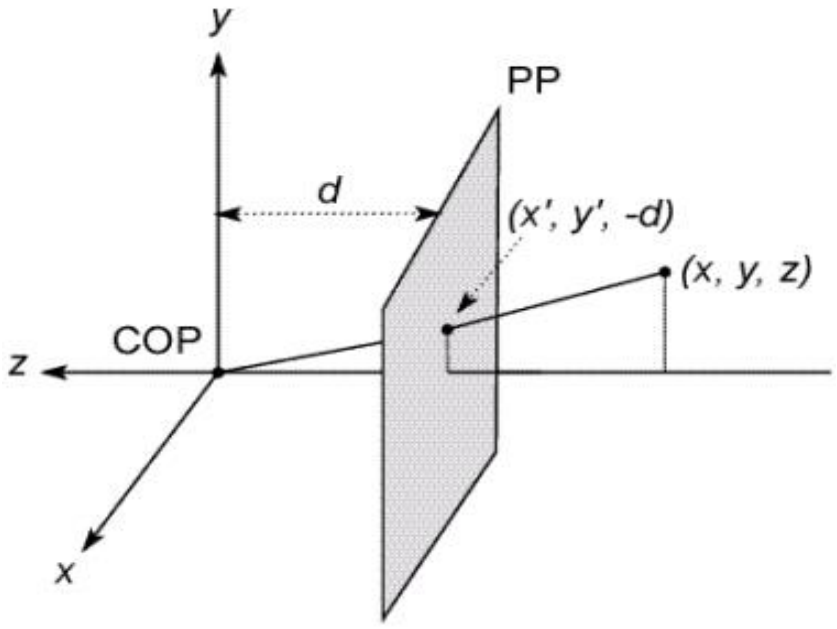

Figure 12. Projection of pinhole camera geometry for the coordinate system.

We are using the pinhole camera model as estimation. The optical centre of the world space coordinates is the centre of projection (COP) at the origin. The projection plane (PP) in front of the COP is the image plane shown through the parallel projection PP (x´, y´, -d). From this point, the camera on z-coordinate point to the negative z axis. Pro-

jections equations is calculated as intersection with the plane PP of ray described from (x, y, z) to COP.

When using similar triangles for smaller distance method, the derivation of the point (x, y, z) becomes:

$$\begin{cases} (x, y, z) \Rightarrow (-d\frac{x}{z}, -d\frac{y}{z}, -d) \\ (x, y, z) \Rightarrow (-d\frac{x}{z}, -d\frac{y}{z}) \end{cases}, \tag{12}$$

where the projection is gotten by throwing out the last coordinate. Therefore, we can keep the distance z and assume a positive focal length. Hence, the projection transformation coordinates (x', y' -d) become:

$$\begin{cases} x' = u = f\frac{x}{|z|} \\ y' = v = f\frac{y}{|z|} \end{cases}, \tag{13}$$

When z is non-linear, the homogeneous image (2D) coordinates and the homogeneous scene (3D) coordinates will become:

$$\begin{cases} (x, y) \Rightarrow \begin{bmatrix} x \\ y \\ 1 \end{bmatrix} \\ (x, y, z) \Rightarrow \begin{bmatrix} x \\ y \\ z \\ 1 \end{bmatrix} \end{cases}, \tag{14}$$

When we convert the orthographic from homogeneous coordinate system equations (14), homogeneous coordinate invariant equations derive under scale in (14) and (15).

Weak perspective in 4-D point and 3-D image position is derived using equation (16).

$$\begin{bmatrix} x \\ y \\ z \\ w \end{bmatrix} \Rightarrow (\frac{x}{w}, \frac{y}{w}, \frac{z}{w}), \tag{15}$$

Hence, when we use homogeneous coordinate system equations (14) as well as projection transformation coordinate equations (15) and (16); we derive the perspective projection matrix in equation (17).

$$\begin{bmatrix} f & 0 & 0 & 0 \\ 0 & f & 0 & 0 \\ 0 & 0 & 1 & 0 \end{bmatrix} \begin{bmatrix} x \\ y \\ z \\ 1 \end{bmatrix} = \begin{bmatrix} fx \\ fy \\ z \end{bmatrix} \Rightarrow (f\frac{x}{z}, f\frac{y}{z}) \Rightarrow (u, v), \tag{16}$$

Perspective effects are not above the scale of each object given, but vary following various points collect into a group at about the same depth. The linear camera calibration model can be written as:

$$\begin{cases} X = x' = \dfrac{a_{11}x_m + a_{12}y_m + a_{13}z_m + a_{14}}{a_{31}x_m + a_{32}y_m + a_{33}z_m + a_{34}} \\ Y = y' = \dfrac{a_{21}x_m + a_{22}y_m + a_{23}z_m + a_{14}}{a_{31}x_m + a_{32}y_m + a_{33}z_m + a_{34}} \end{cases}, \tag{17}$$

where $a = [a_{11} \ldots a_{34}]$ are the scaling of the coefficients respectively to the perspective transformation matrix (X, Y), with the value $a_{34} = 1$. Finally, the system equations (18) can be joined into the verification model:

$$\begin{bmatrix} X \\ Y \end{bmatrix} = \begin{bmatrix} x_m\ y_m\ z_m\ 1\ 0\ 0\ 0\ 1 - Xx_m - Xy_m - Xz_m \\ 0\ 0\ 0\ 0\ x_m\ y_m\ z_m\ 1 - Yx_m - Yy_m - Yz_m \end{bmatrix} \begin{bmatrix} a_{11} \\ a_{12} \\ : \\ a_{33} \end{bmatrix}, \tag{18}$$

For every point pair $\{(x_{m,i}, y_{m,i}, z_{m,i}), (X_i, Y_i)\}$, they involve two algebraic system equations (19), for the unknown coefficient vector $a = [a_{11} \ldots a_{33}]^T$ of the type stated in the equation (18). Since columns are linearly dependent, the coefficient matrix collected on the right hand side of the equations (17) will be singular.

3.7.3 Nonlinear Camera Model/Lens Distortion Model

The perfect linear model described is not notified because the real cameras and lenses support different aberrations. The various types of defects in the conception and assemblage of lenses linked to the camera's optical system are the fundamental origins of error. Furthermore, in Weng's tests, there are three types of distortion mentioned which are as follows (from Figures 13 and 14): an inaccurate lens shape which shows only radial position error is the first type of distortion. Incorrect lens assembly which produces both radial and tangential errors in different point locations are usually as a result of other types of distortion.

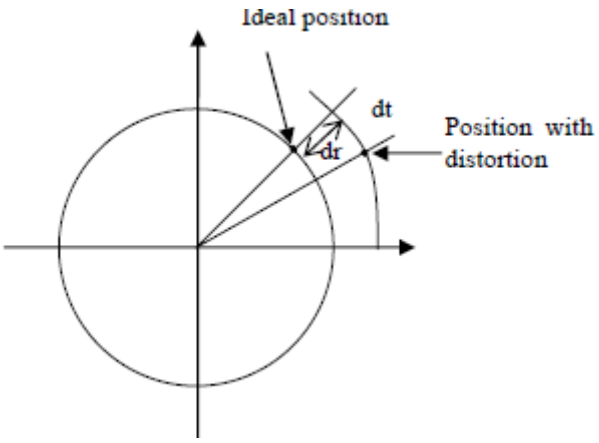

Figure 13. Ideal position describes by radial and tangential distortions.

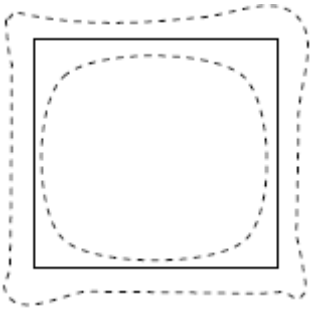

Figure 14. Radial distortion: solid lines = no distortion, inner dashed line = barrel distortion, outer dashed line = pincushion distortion.

Applying imperfect lenses to the best possible position causes radial distortion as seen in figures 13 and 14. Therefore, for rays that pass through the edge of the lens we often observe shifts. The total distortion model is shown in equation (20) below.

$$\begin{cases} \delta_x(X,Y) = (g_1 + g_3)X^2 + g_4XY + g_1Y^2 + k_1X(X^2 + Y^2) \\ \delta_y(X,Y) = g_2X^2 + g_3XY + (g_2 + g_4)Y^2 + k_1Y(X^2 + Y^2) \end{cases}, \tag{19}$$

where $\delta_x(X,Y)$ and $\delta_y(X,Y)$ are the distortion models, X and Y are the distorted coordinates, the coefficients $\{g_1, g_2, g_3, g_4\}$ are the set of distortion model parameter, and the coefficients $\{k_1,k_2\}$ are the set of radial symmetric distortion parameter.

The image radial distortion is represented by the third-order polynomial in equation (18). The below system equations show the absolute nonlinear camera model with distortions.

$$\begin{cases} X + (g_1 + g_3)X^2 + g_4XY + g_1Y^2 + k_1X(X^2 + Y^2) = \dfrac{a_{11}x_m + a_{12}y_m + a_{13}z_m + a_{14}}{a_{31}x_m + a_{32}y_m + a_{33}z_m + a_{34}} \\ Y + g_2X^2 + g_3XY + (g_2 + g_4)Y^2 + k_1Y(X^2 + Y^2) = \dfrac{a_{21}x_m + a_{22}y_m + a_{23}z_m + a_{14}}{a_{31}x_m + a_{32}y_m + a_{33}z_m + a_{34}} \end{cases}, \tag{20}$$

where X and Y are the distorted coordinates, the coefficients $\{k_1, g_1, g_2, g_3, g_4\}$ are the set of distortion parameter.

In the equation (20), any nonlinear algorithm used for radial distortion calibration, usually have algorithm issues of convergence and stability. Faig, (1975), put forward a two-step method which concerns implementing distortion requirements from any iteration as mentioned: The first is the non-iterative algorithm made from the direct calculation of closed-form result for the external parameters and the second is the significant internal variables based on a distortion-free camera model. Hence, a camera model that comprises distortion using the solution of the non-iterative algorithm as an initial estimate is the basis for nonlinear optimization.

4 SPECTRAL IMAGING AND DESIGN

4.1 Background and Theory

The transient change of light which is conveyed through tissue is carried out by the principle of photon connection spectroscopy which is an imaging technique called Diffuse Correlation Spectroscopy (DCS). Since the 1970's effective light scattering or photon correlation spectroscopy technique has been applied and was first used to analyse the flow of molecular movements in solutions. Therefore, the casual autocorrelation capacity of scattered light is analysed using DCS. (Durduran, et al., 2004).

The test setup and the material through which the photons spread determine the way light scatters. In this step we first depict single scattering postulation and then move to further physiologically notable different multiple-scattering mode. When the scatters inside the medium are particles like items that move, the intensity of light collected by an identifier will change after some time. Therefore, intensity variations transfer data about the movement of the particles. Hence, autocorrelation is the best way the data is perceived. (Suresh & Sujatha, 2011).

The autocorrelation function denotes a technique that appears variations in the refractive indicator and interface the scattering intensity (I) of a particle at time t, with its scattering intensity of time delay ($t+\tau$), when the particle emitted causes constantly the movement in the coordinate system. This principle acted in single scattering medium tissues is found in Equation (22):

$$A_2(\mathrm{q},\tau) = \frac{I(q,t)\cdot I(q,t+\tau)}{I^2}, \tag{21}$$

where $A_2(q,\tau)$ is the intensity autocorrelation function for a wave vector q, τ is the delay time, $I(q,t)$ is the intensity of a particle. Assuming Brownian motion, on the other hand, we can rewrite equation (23) as:

$$A_2(q,\tau) = 1 + e^{-2D_B q^2 \tau}, \tag{22}$$

where q^2 is defined as the square of the scattering wave vector (contained waves number and the angle comprised between the source and detector).

4.2 Diffuse Reflectance Spectroscopy

An optical technique Diffuse Reflectance Spectroscopy (DRS) uses visible and near infrared light with a wavelengths range of 400-1500 nm in getting the quantity of the hemoglobin concentration and oxygenation of blood in surface (less than 1mm depth) vessels. Therefore, the DRS device is basically composed of an optical fiber package with arbitrarily scattered source and detector fibers. (Papazoglou, et al., 2008).

From Figure (15), white light from the original source will be reflected, transmitted, absorbed or scattered when entering the tissue. When each light is moreover reflected from the specular reflection or is scattered inside the skin surface, it will be sent by the indicator fibres to a spectrometer. In general, the light is dispersed into a spectrum using a spectrometer and is examined using a photodetector exhibit or CCD chip and regenerated to an electrical signal. (Weingarten, et al., 2006).

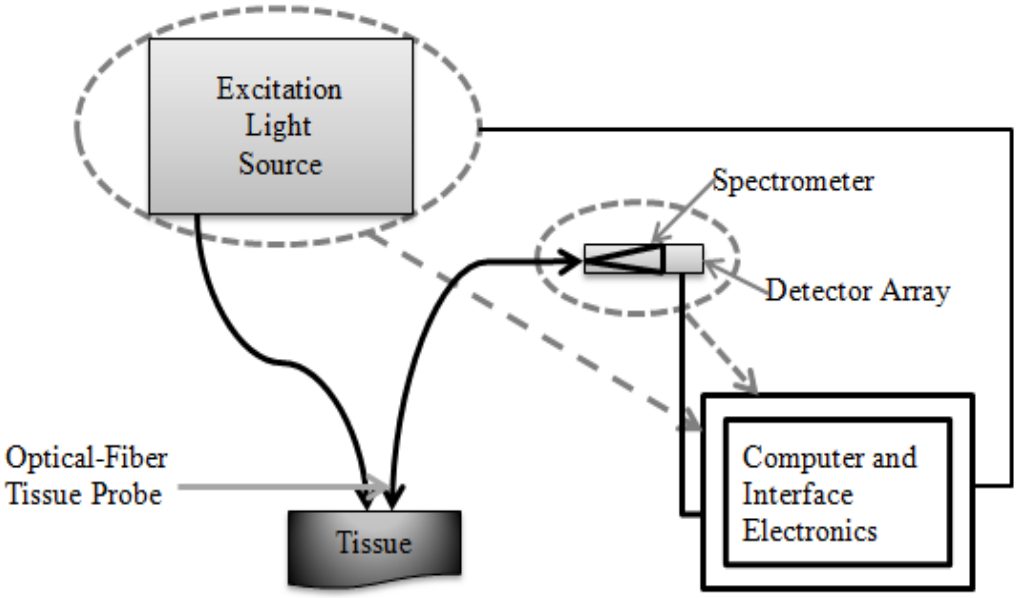

Figure 15. Diffuse reflectance spectroscopic system. The light source emits broadband light in visible and NIR range. (Mourant & Bigio, 2003).

The reflected light spectrum and intensity is used to get the quantity of certain absorbing particles in the tissue. The particular wavelength examined determines if it is oxygenated hemoglobin, deoxygenated hemoglobin, water and different organic chromophore comprised in the human body. (As illustrated in Figure 16 for assimilation spectra).

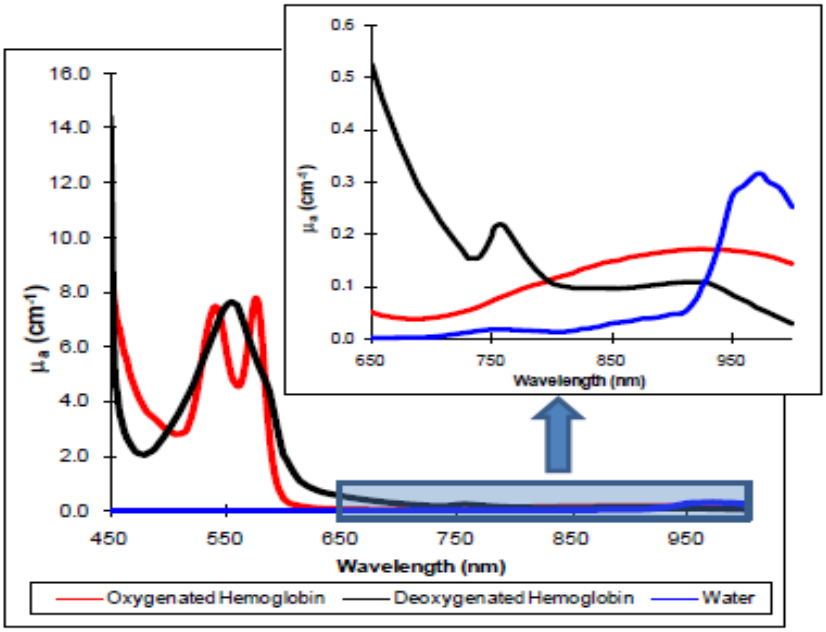

Figure 16. Extinction of hemoglobin and water in the wavelengths range of 450-1000nm based on hemoglobin absorption applied coefficients. (Prahl, 1998).

Identifying the wavelengths being the most important assimilated which more existed chromophores; is achieved by the reflectance spectrum which is usually converted to an absorbance spectrum. Therefore, it is required in this process to calibrate the system with a pure white specimen in the entire wavelengths range for reflectance and a pure dark specimen in the entire wavelengths range for absorbance. In addition, the calculation of absorbance spectrum is defined as:

$$A(\lambda) = -\log_{10} \cdot \left[\frac{I(\lambda)}{I_{ref}(\lambda)} \right], \tag{23}$$

where the absorbance range $A(\lambda)$ is derived by computing the inverse logarithm of the proportion of the intensity signal measurement $I(\lambda)$, to the reference power signal $I_{ref}(\lambda)$.

4.2.1 Reflection Spectra Technique

Diffuse reflectance occurs when a light emission is incident on a turbid medium, for example, a tissue which endures different scattering and absorption and a portion of it is re-transmitted from the tissue surface. When we measure from a given specimen the wavelength and intensity of absorption of near-ultraviolet and visible light this is known as ultraviolet-visible spectroscopy. However, the movement of the external electrons to higher energy orbital levels are achieved by the ultraviolet and visible light which are energetically sufficient to do so. Determining the concentration of analytic in tissue and measuring the absorbance at some wavelength is determined by applying the Beer-Lambert Law. UV measurements uses hydrogen as light source and a tungsten lamp is used for visible measurements. (Prahl, 1998).

Furthermore, from initial source we can use a prism to select a wavelength from continuous light sources. Hence, we can derive the spectra by scanning the wavelength separator and quantitative measurements made from a spectrum or a single wavelength. The laws of light absorption kept for analytical purposes are defined by two main proposals. The first, the intensity of the source light sent is independent of the proportion of incident light absorbed by a transparent medium, this describes the Lambert's Law mentions.

$$T = \frac{I}{I_0}, \tag{24}$$

where T is the transmittance ratio of transmitted to incident intensity, I is the intensity of the source light transmitted, and I_0 is the intensity of the incident light absorbed by a transparent medium.

The second, Beer’s Law states that both the concentration of the absorbing medium and the thickness of that medium are correlative to the absorption of light. Hence, when we combine the two propositions we get the Beer-Lambert Law which gives the link be-

tween absorbance and transmittance. Monochromatic light which is a single wavelength verifies the Beer-Lambert law.

$$A(\lambda) = \int_{I_0}^{I} \frac{-1}{I} dI = \ln\left(\frac{I_0}{I}\right) = \varepsilon(\lambda) \cdot c \cdot l, \tag{25}$$

where $A(\lambda)$ is the absorbance referred to as the loss in light intensity, ε is the molar attenuation coefficient of the medium, c is the molar concentration, and l is the path length.

The capacity of the system to contrast one subject with another is constrained by the relative idea of this innovation. One point to notice is that when the infiltration depth is around 1 mm, the DRS method is applied for using wavelengths range in the visible between 500 to 650 nm scales. As illustrated in this section, since the high extinction (greater than 2 cm^{-1}) results in light not being returned at profundities excess 1 mm, the Diffuse NIR Spectroscopy (DNRS) and DCS optical systems applied in this study cannot utilize these wavelengths. Therefore, changing the wavelengths to the 680-900 nm scale in the diffuse near infrared reflectance spectroscopy (DNIRS) and DCS systems can be done to carter for this limit. (Weingarten, et al., 2008) (Papazoglou, et al., 2008).

Evaluation of peripheral blood vessel occlusive trouble has been achieved using the Diffuse Reflectance Spectroscopy DRS with readings measured at specific intervals from 0-240 seconds. Therefore, the computation of the extinction was achieved using original spectra of oxygenated and deoxygenated hemoglobin. (Bykowski, et al., 2004).

4.3 Hyper Spectral Imaging

Obtaining a sequence of each pixel in the frame images demonstrate the energy of spread reflected light from natural tissue at given discrete wavelengths λ describes hyper spectral imaging. Therefore, hypercube, referred by $H(x, y, \lambda)$ defines the derived set

of images contained in one frame for analysis, where x and y denoted the two spatial directions coordinates and λ is the spectral band coordinate. The diffuse reflectance range of the tissue at an area (x, y) relates to each pixel obtained from the frame image in a hypercube. The particular concentration of tissue chromophores obtained from human blood cells, like melanin or hemoglobin is displayed from the hypercube testing. Hence, hyperspectral imaging is a derived method from the spatial diffusion of oxygen saturation in the skin surface for the visible and near-infrared spectrum (Zuzak, et al., 2002).

Therefore, the local absorption of the tissue by the adjusted Beer-Lambert law is expressed in the equation (28):

$$A(x, y, \lambda) = -\log_{10}\left[\frac{I_t(x, y, \lambda) - B(x, y, \lambda)}{I_c(x, y, \lambda) - B(x, y, \lambda)}\right], \tag{26}$$

where $I_t(x,y,\lambda)$ is the hyperspectral image of the analysed tissue, $Ic(x,y,\lambda)$ is the reference image, $B(x,y,\lambda)$ is the dark image with the closed hermetically lens, (x,y) are pixel coordinates, and λ is the band coordinate (wavelength).

The spectroscopy method used to estimate cutaneous oxygen in the human skin and take a 2-dimensional detail of oxygenation measurements is referred to as hyper spectral imaging (HIS). The main theory is close to the Diffuse Reflectance Spectroscopy DRS system. A single origin point we obtain an absorbance spectrum which is sharply differs from (DRS), HSI takes several spectra over a large (for instance, 400×460 pixels resolution) focal or central plane. HSI unit derives from a wideband light origin and extends from visible wavelengths which brighten the skin tissue which is similar to the DRS system. (Bykowski, et al., 2004) (Kong, et al., 2004).

Intensity at each wavelength is incorporated making use of a camera with a controllable optical filter used to choose distinct advantageous wavelengths and then it stacks the images over one other to protect the spatial alignment. Similar to DRS, a white source is

used to calibrate relative absorbance spectra of oxy- and deoxyhemoglobin and the plotting of the approximated values of ordinarily oxygen saturation, SO_2 for every pixel can be done over an anatomical guide. The infiltration depth is limited to some hundred microns due to the fact that this is a reflectance based technique, (Kocsis, et al., 2006) (As illustrated in Figure 18).

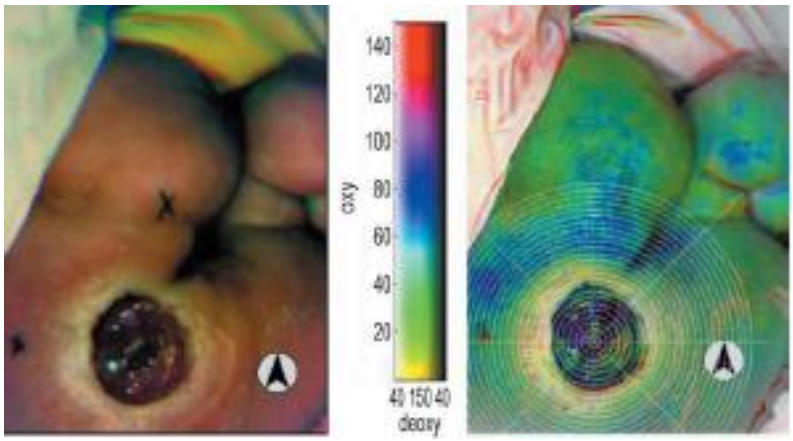

Figure 17. A diabetic foot ulcer with normal in colour image (left) and hyperspectral image (right). The colour describes oxy-hemoglobin values and brightness describes deoxy-hemoglobin values. (Khaodhiar et al., 2007).

Hyper spectral imaging can be applied in several areas such as airborne control detecting and remote device used to sustain quality. Since the middle 2000s, it has been applied in the examination of perpetual injuries. Furthermore, a report applied HSI in monitoring hemoglobin fixations at a few time which focuses along the patching procedure of a diabetic ulcer. Therefore, in a report from 2007, the capability of HSI to separate recovery ulcers from non-healing ones in view of the steps of oxy- and deoxyhemoglobin steps in the injuries with both notably larger in non-healing versus healing was demonstrated. The recovery in diabetic ulcers with 93% scale of accuracy and 86% particularity was estimated in this process. As pointed out, in the report, it was stated that deoxyhemoglobin probabilities values were factually ($p < 0.005$) higher from Peripheral Arterial Disease (PAD) on the plantar skin for limbs secure contrasted than other parts without PAD. The restricted infiltration depth of some hundred microns of the

system is most probably the reason for the incapacity to recognize PAD in all surfaces or different wavelengths. (Zuzak, et al., 2002) (Gowen, et al., 2007).

4.3.1 Medical Hyper Spectral Imaging

Hemoglobin is known as oxyhemoglobin and deoxyhemoglobin, respectively when it is in its oxygen-limited and unrestricted composition. Hemoglobin is the group of atom contained in blood that takes charge of taking oxygen from the lungs to the rest part of the body which leads to the relaxation of the body. However, the proportion of oxyhemoglobin concentration to the entire hemoglobin blood is referred as oxygen saturation implies SO_2. (Kocsis, et al., 2006).

SO_2 represents the indication of oxygen that is conveyed to the tissues and used by it. The optical assimilation factor of oxyhemoglobin are different notably from deoxyhemoglobin. Therefore, the concentration and oxygen saturation of hemoglobin inside the tissue determines the extinction spectrum of tissue. Moreover, its diffuse reflectance spectrum is alternated by the changes inside the tissue's spectral extinction factor. Hence, using the hyper spectral imaging method, we can measure the hemoglobin concentration and oxygen saturation from the tissue's diffuse reflectance which is represented as transcutaneous tissue oxiometry (TcpO2). (Finlay & Foster, 2004).

For example, in the visible range we have hemoglobin extinction spectra of the tegument. In addition, in the ultraviolet (UV) spectrum we have notable extinction of light by melanin in the epidermis and less in the visible spectrum. Therefore, the spectral molar extinction coefficients of melanin, oxyhemoglobin, and deoxyhemoglobin as stated in the literature is summarised in Figure 18. In conclusion, we can use two wavelengths for sufficient approximation of SO_2 saturation. For a typical oxiometry it uses just 660 nm and 910 nm. (Prahl, 1998).

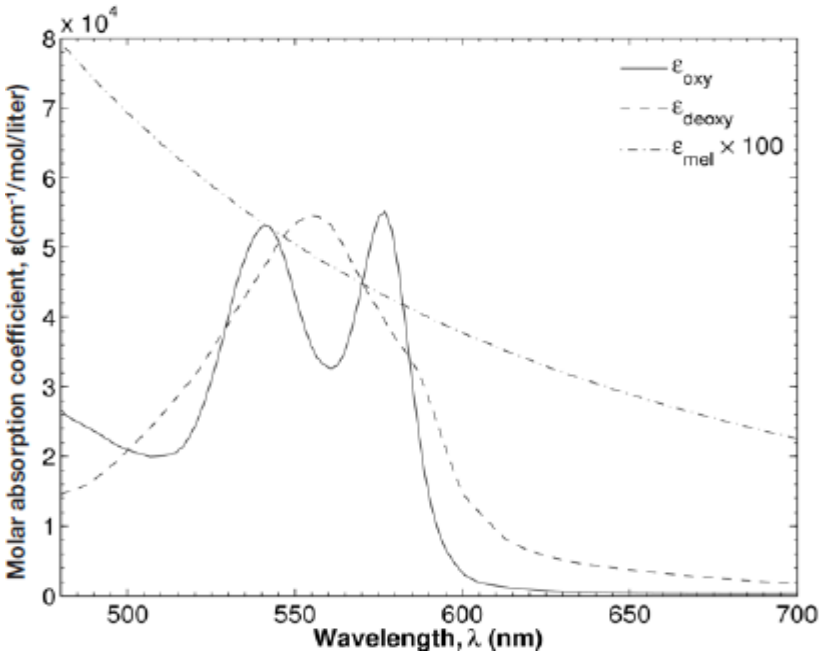

Figure 18. Absorption spectra of melanin, oxyhemoglobin and deoxyhemoglobin in the visible range.

A particular extinction peak for spectral molar is about 554 nm characterized by deoxyhemoglobin while oxyhemoglobin shows the extinction peaks of wavelength range between 542 to 578 nm. Reflectance spectroscopy is derived from several variations, which aids image of microcirculation and sectional oxygen saturation derived of the liquid blood in neuropathic feet. (As illustrated in Figure 18).

Oxyhemoglobin, deoxyhemoglobin and water are the main chromophores components derived in tissue located into the range's near-infrared between 685 nm and 830 nm. Therefore, by taking measurements of both the reduction in signal amplitude and variation in phase of the single wavelength the extinction coefficients for these chromophores are derived. Hence, evaluating the optical absorption (μa) and reduced scattering (μs') coefficients of the tissue from developed theory above that allows this computation. (Prahl, 1998) (Zijlstra, et al., 1991).

Based on optical absorption in the wound patient, the concentrations of hemoglobin and water concentrations can be calculated using the following equation:

$$\varepsilon Hb\lambda[Hb]+\varepsilon HbO_2\lambda[HbO_2]+\mu_a^{\lambda},H_2O\lambda[\%H_2O]=\mu_a^{\lambda}, \quad (27)$$

where $\varepsilon Hb\lambda[Hb]$ *and* $\varepsilon HbO_2\lambda$ *[*HbO_2*]* are the molar absorption coefficients of deoxyhemoglobin and oxyhemoglobin respectively, μ_a^{λ}, $H_2O\lambda$ is the optical absorption coefficient of pure water, μ_a^{λ} is the optical absorption, and $[\%H_2O]$ is the percentage of water in the evaluated tissue which is placed at 70%. Total hemoglobin (*Hb*tot) can be computed by adding oxyhemoglobin and deoxyhemoglobin. (Khaodhiar et al., 2007).

Estimation of the spatial dispersion of oxygen saturation in human skin and evaluating the circulatory changes in the diabetic foot is achieved using hyper spectral imaging in the visible and near infrared parts of the spectrum. Therefore, using a hyperspectral camera we can acquire these hyperspectral images as 12-bit digital data hypercubes. Several parameters like $C_{oxy}(x,y)$, $C_{deoxy}(x,y)$, and $G(x,y)$ affects the apparent absorption in cutaneous tissues. The latter one is not dependent on wavelength, and the light scatted on the tissue outside of ROI is taken into account. (More, 1978) (Nouvong, et al., 2009).

The apparent absorption derives from spatial coordinate for absorption distribution by the tissue applying Beer-Lambert law as shown equation (28):

$$A(x,y,\lambda_j)=G(x,y)+S\cdot C_{oxy}(x,y)\cdot\varepsilon_{oxy}(\lambda_j)+C_{deoxy}(x,y)\cdot\varepsilon_{deoxy}(\lambda_j), \quad (28)$$

where $A(x,y,\lambda_j)$ is the apparent absorption of the tissue, $G(x,y)$ is the factor independent of wavelength for any light scattering by the skin, ($C_{oxy}(x,y)$, $C_{deoxy}(x,y)$) are oxyhemoglobin and deoxyhemoglobin concentrations respectively, ($\varepsilon_{oxy}(\lambda_j)$, $\varepsilon_{deoxy}(\lambda_j)$) are oxyhemoglobin and deoxyhemoglobin spectral molar extinction coefficients respectively, and *S* is the scaling coefficient for the whole image.

5 EXPERIMENTS AND RESULTS

5.1 Overview

The aim of this thesis is to develop a system able to provide thermal and spectral images and body temperature measurements without being intrusive and uncomfortable. Because infrared and near–infrared light work like visible light, measurements ought to be done inside a cardboard box that blocks ambient light.

By using the system in figures 19 and 20, contact and non-contact temperature sensor plays an important role for body temperature measurement. The body temperature is measured by contact temperature sensor and sent by a microcontroller to PC in real time. The smartphone plays the role of communication scheme. It accomplishes the following tasks sequentially: take normal foot images with different illumination and take thermal images. It sends the images to the PC by wireless communication; where the image files will be displayed on the interface. At this stage, the PC can perform, process, and analyse the image files obtained by using algorithmic computation from MATLAB software environment. A spectral image is created from the images with different illumination, which is accomplished by monochromatic LED's.

It is important to measure the subject's body temperature accurately as well as the humidity of experiments testing area. A temperature sensor detects the subject body temperature from the arm and another sensor the ambient temperature and humidity also in real time.

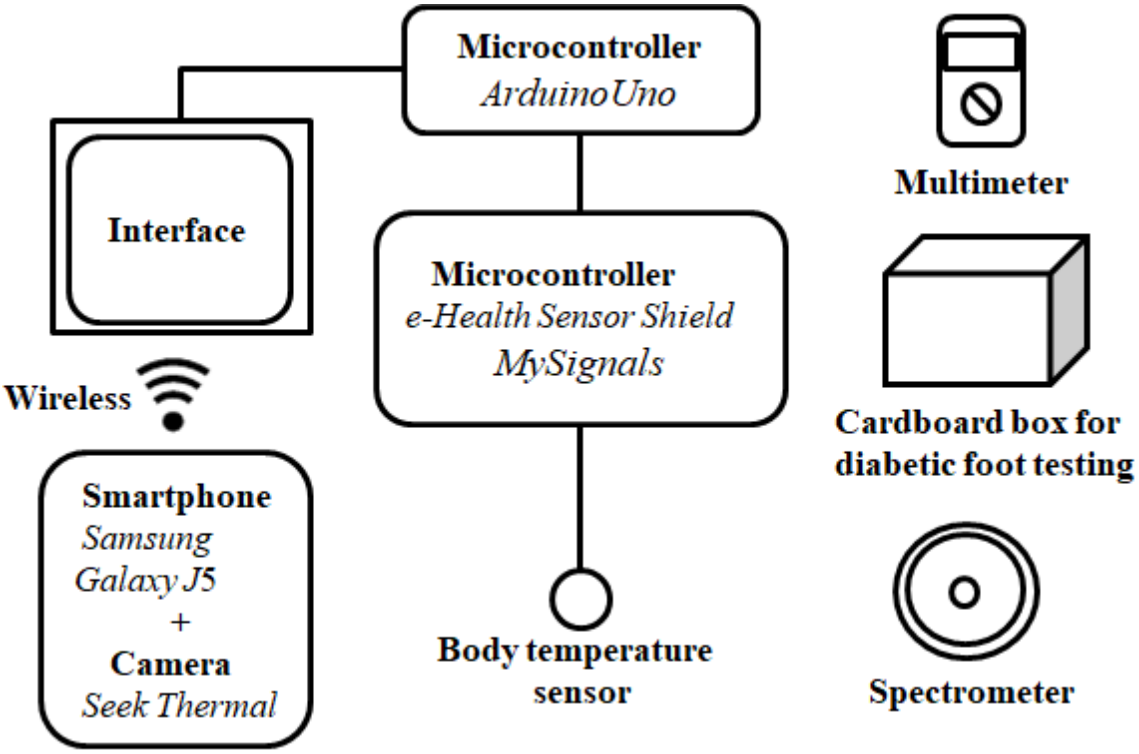

Figure 19. Block diagram of system design for thermal imaging and contact body temperature.

5.1.1 Equipment

The proposed system includes a thermal camera (*Seek thermal compact*) connected to a smartphone *Samsung Galaxy J5*, which is used to acquire infrared thermal images. This thermal imaging system (smartphone and thermal camera) is used to compute the temperature and spectral temperature gradient and variations, which can indicate a possible evolution of diabetic foot.

Hence, system design implementation is done with the connection of a set of components shown in Figure 20 during the experiments phase as described with more details in sections 5.2.

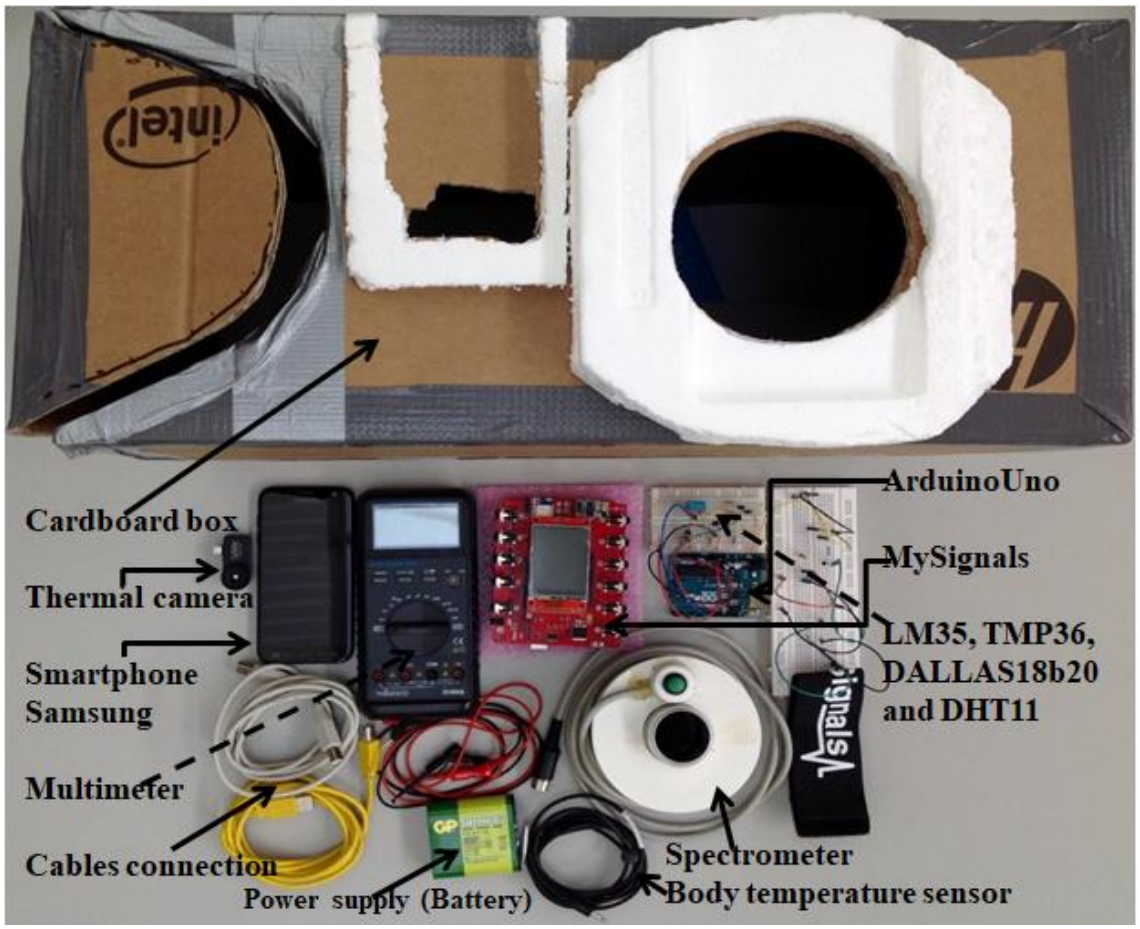

Figure 20. System design implementation.

Arduino Uno is the smart micro-controlling unit programmed with the Arduino software. This unit does not require any other software rather than Arduino for installing. Arduino is open source hardware board with different open source libraries for interfacing it on board with other external components such as LED, LCD and sensors. The integrated circuit (IC) used on the Arduino Uno is named ATmega328.

MySignals is development board hardware for medical devices used to develop eHealth applications or even to add sensors to build new medical applications like monitoring body temperature data, monitoring ECG signals or monitoring EMG signals. MySignals uses *libelium* software environment which is open source software with different open source libraries for interfacing it on board with other external components.

LM35, TMP36, and DALLAS18b20 are the low-cost analog and digital precision integrated-circuits (IC) temperature sensors. The output voltage of those sensors are linear as for voltage versus Celsius temperature (every 1 °C increases the output voltage by 10 mV). Thus, DHT11 is considered as an ultra-low-cost digital temperature and humidity sensor. It uses a thermistor and a capacitive humidity sensor to measure the surrounding air, and spits out a digital signal on the data pin.

LED lighting unit with four set of monochromatic to monitor RGB and NIR channels obtained with adjustment of 4 resistors respectively of 11 Ω, 18 Ω, 47 Ω, and 50 Ω. Thus, each resistor is connected in series to a power supply or to a battery of power intensity is 5V. Mobile phone *Samsung J5* combined to a thermal camera *Seek Thermal* to obtain thermal images colour, and NIR images are obtained by using *iPhone 5SE* with *NIR Color* software application.

5.2 Tests Procedures

The feet of the subjects were cleaned dry and rested for 2 to 5 minutes to stabilize blood circulation after physical activities in the beginning ($t = 0$) and at the end of each experiment ($t = T$). Foot thermal images and spot temperature were captured from both right and left foot of the subject. In the beginning of each measurement, the thermal camera was calibrated using uniform thermal distribution of the cardboard box surface for the testing subjects' feet. On the other hand, contact temperature sensor detects the subject body temperature accurately and humidity of testing area and obtains both data in real time. These body temperature sensor and IC temperature sensors will transmit the data directly to microcontrollers (Arduino Uno and MySignals), which are connected to the PC by USB port.

The thermal camera connected to the smartphone and the spectrometer (mobile phone camera + LEDs) are placed in two holes on the testing cardboard box, which is placed in a closed room with stable and intrusive room temperature where in the experiments were done. Thermal cameras are passive sensors that capture the infrared and near-

infrared radiation emitted by both subjects' feet with the body temperature variation emitted spontaneously electromagnetic radiation on the ROI, and may be regulated from variations of ambient temperature. By using the spectrometer, LEDs with different colours are deployed one by one and an RGB colour image is captured with every colour. Ice is used to monitor the thermoregulation dynamics from the blood circulation to the feet for a limited sequence of experiments; namely 1min of normal state and 1 min disturbance by ice, 5 min of imaging-thermal/spectral for both feet (left and right) and 5 min of spectral images (sequence of Red + Green images, sequence of Red + Blue images, sequence of Green + Blue images, sequence of Red + NIR images, sequence of Green + NIR images and sequence of Blue + NIR images). This protocol is done with RGB+NIR before and after ice.

5.3 Thermal Image Analysis Methods

The thermal image methods based on a developed system should be implemented with the thermal visualization of both feet by a smartphone *Samsung Galaxy J5* and a thermal camera *Seek Thermal* to capture the subject's images which appear the temperature values obtained from the human body temperature and the experimented ROI. This theory explained in sections 3.4 and 3.7 is applied here by thermal image analysis.

In this stage, the detailed method is shown on the Figure 21 below with the analysis of few lines of code mainly used for thermal image implementation.

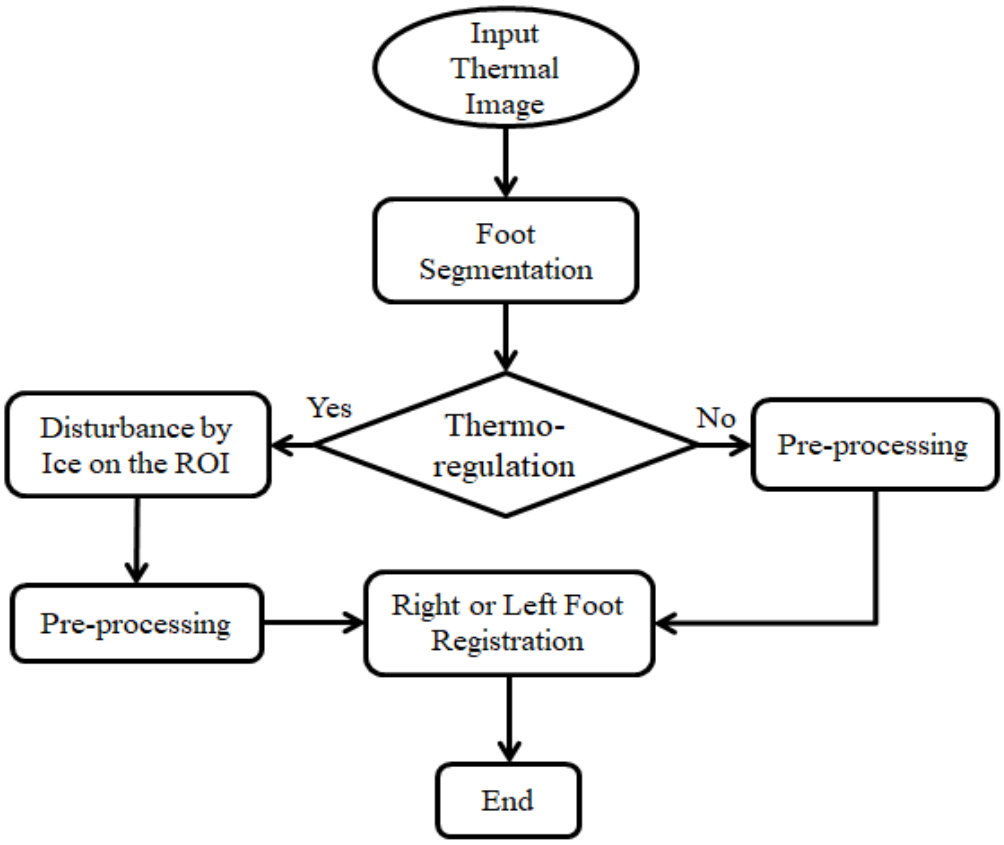

Figure 21. Flowchart of thermal image analysis.

Following the flowchart of thermal image, we have implemented reading of thermal temperature from the thermal image and the thermal's video frame. In order to estimate the mean and standard deviation of the thermal temperature for the experimented subject's feet.

In this step, we compute different minimum and maximum temperatures in several frames respectively from thermal video and thermal image. Conversion from gray value to temperature based on the scale that appears on thermograph.

```
%define position of thermoregulation on the subjects' foot
rectangle('Position',[ROI_left, ROI_up, ROI_width, ROI_height])
drawnow
Tmin = input('Minimum temperature:');
Tmax = input('Maximum temperature:');

T1 = rgb2gray(frame1);
T1 = Tmin+((Tmax-Tmin)/255)*rgb2gray(frame1);
```

```
figure(2)
image(T1)
colormap(gray(255))
impixelinfo()

rectangle('Position',[ROI_left, ROI_up, ROI_width, ROI_height])
drawnow
title('ROI - Position')
ROI_T1 = T1(ROI(1,2):ROI(2,2), ROI(1,1):ROI(2,1));
ROI_Tave(1) = mean(ROI_T1(:))
ROI_Tstd(1) = std(double(ROI_T1(:)))
```

In the loop, thermal temperatures found to the ROI of any thermal image e.g. (ThermalLeft1_before.jpg) have been read frame by frame from thermal video (JohbVideo_1.mp4). Mean and standard deviation values of the ROI are plotted with respect to the frame number. Next, we defined the ROI with location (left, up, width and height). By selecting manually maximum and minimum temperature from the desired location of the ROI, selected image appears to the output.

```
%define new frame and new temperature
Tmax2 = 31;
Tmin2 = 20;
frame2 = readFrame(JohbVideo_3);
T2 = Tmin2 +((Tmax2 - Tmin2)/255)*rgb2gray(frame2);
Tave = mean(mean(T1(600:799, 300:499)));

% loop proceed temperature analysis frame by frame contained in the
video while comparing them with thermal temperature

k = 1;
while hasFrame(JohbVideo_1)
    mov.cdata = readFrame(JohbVideo_1);
    frame1=mov.cdata;
    ROI_T1 = T1(ROI(1,2):ROI(2,2),ROI(1,1):ROI(2,1));
    ROI_Tave(k) = mean(ROI_T1(:));
    ROI_Tstd(k) = std(double(ROI_T1(:)));
    k = k+1;
end
```

5.4 Spectral Imaging Methods

The spectral imaging methods based on a developed system have been implemented with the spectral visualization of both feet by using RGB + NIR spectrum LED lighting

in the cardboard and a smartphone *iphone 5SE* with *NIR color* application to capture the subject's images of feet. This theory explained in sections 4.2 and 4.3 is applied here by spectral imaging.

In the following, the detailed method is shown on the Figure 22 below with the analysis of few lines of code mainly used for spectral imaging implementation.

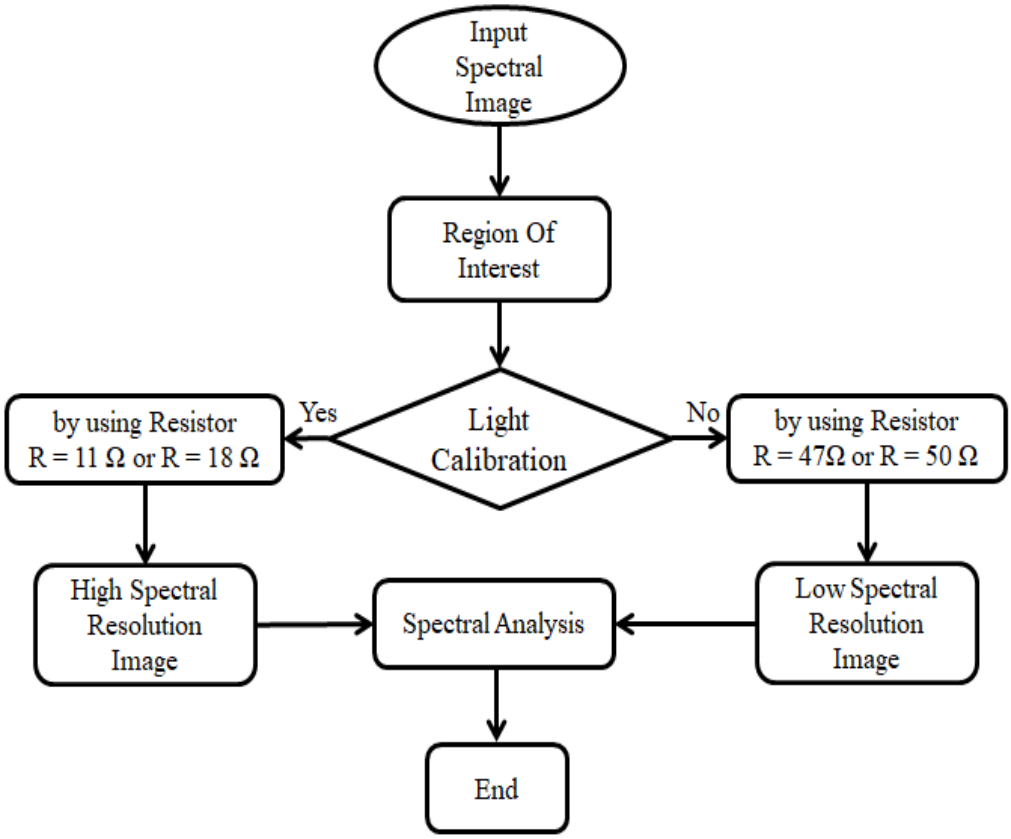

Figure 22. Flowchart of spectral image analysis.

Next, we computed step by step spectral images and channels from signal spectral, temporal dynamics, temporal change between channels, spatial coordinates for channels, extraction of images from channel, average of channels, and estimation of the different spatial variations between channels.

In this step, we have combined several spectral images between two channels by using principle component analysis and respectively Red, Green, Blue and NIR channels in the spectrum.

```
%Compute Spectral images

R_G = uint8((double(R)-double(G))/2 + 128);
R_B = uint8((double(R)-double(B))/2 + 128);
G_B = uint8((double(G)-double(B))/2 + 128);
R_NIR = uint8((double(R)-double(NIR))/2 + 128);
G_NIR = uint8((double(G)-double(NIR))/2 + 128);
B_NIR = uint8((double(B)-double(NIR))/2 + 128);

% Thermoregulation dynamics of 2 appeared channels by using ice
%Compare spectral images before and after with Ice

delta_R_G = uint8((double(R2_G2)-double(R_G))/2 + 128);
figure(19)
image(delta_R_G)
colormap(jet(256))
title('Spectral of Red-Green: after ice - before ice')
```

Difference of two different spectral images respectively used from (Red and Green) channels before and after applied thermoregulation dynamics.

5.5 Registration of Thermal and Spectral Images

The image fusion process was the technique used to implement the registration of thermal and spectral images, where images were combined together in different scales after multiple scale decomposition occurred after pre-processing step. The final image fusion was the result of boundary detection checking made in the image synthesis step. This theory explained in sections 3.5, 3.6 and 3.7 is applied here by registration of thermal and spectral images.

In the following, the detailed method is shown on the Figure 23 below with the analysis of few lines of code mainly used for image fusion.

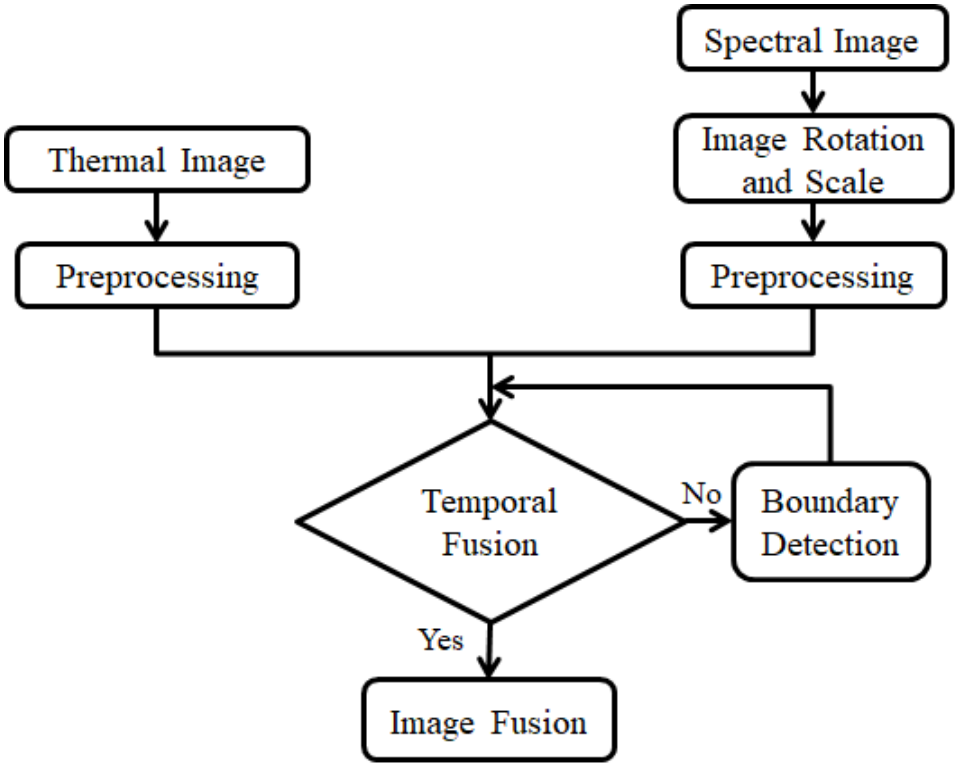

Figure 23. Flowchart of thermal and spectral images fusion.

In this stage, we combined thermal and spectral images for RGB regions with different pixels, wavelength and texture in such of way to create an image fusion.

```
%size and position of channel

NIR = rgb2gray(Nir_bef);
size(NIR)
THERM = rgb2gray(Thermal_bef);
size(THERM)
diff=size(THERM)- size(NIR);
NIR = padarray(NIR,diff, 'post');
disp(size(NIR));
disp(size(THERM));
disp("DEBUG ENDS")
NIR_THERM = (double(NIR)+double(THERM))/2 + 128;

%Combine to 2 different channels Red_ice and Green_ice

diff=size(THERM2)- size(NIR2);
NIR2 = padarray(NIR2,diff, 'post');
disp(size(NIR2));
disp(size(THERM2));
disp("DEBUG ENDS")
NIR2_THERM2 = uint8((double(NIR2)+double(THERM2))/2 + 128);
figure(27)
image(NIR2_THERM2)
```

```
colormap(jet(256))
title('Spectral image Blue + THERM, after ice')

%Combine to 2 different spectral images before and after with Ice

sum_NIR_THERM = uint8((double(NIR2_THERM2)+double(NIR_THERM))/2+128);
figure(37)
image(sum_NIR_THERM)
colormap(jet(256))
title('Sum of NIR-THERM: after ice + before ice')
```

The main objective of both steps was to combine respectively two spectral images and different channels in way to obtain respectively an image fusion and a channel fusion combining pixels and initial textures.

5.6 Tests and Results

For the thermal image analysis, the experimental test were realized on the three subjects of different texture and skin colours in way to improve the accuracy result and minimize error rate of approach between the different subjects as shown in the figures above.

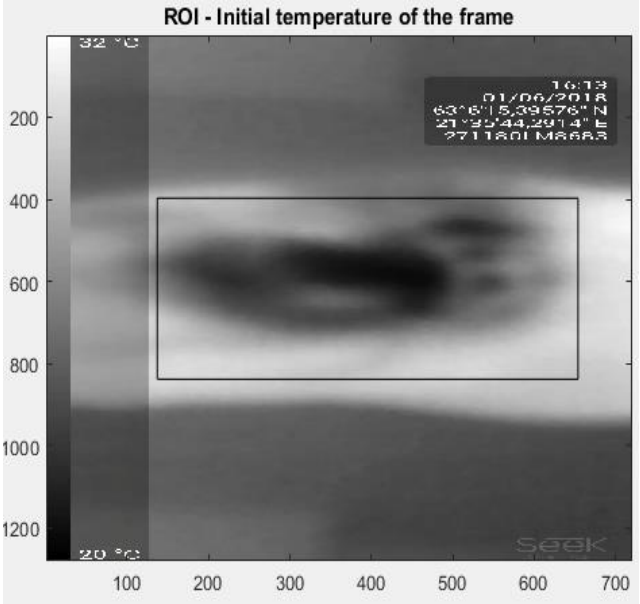

Figure 24. Initial temperature on the frame of the ROI observed on the subject 1 after applied thermoregulation dynamic.

In the figure 24, the ROI is located in the portion of ice disturbance between range of [380, 840] for y coordinate and range of [140, 670] for x coordinate.

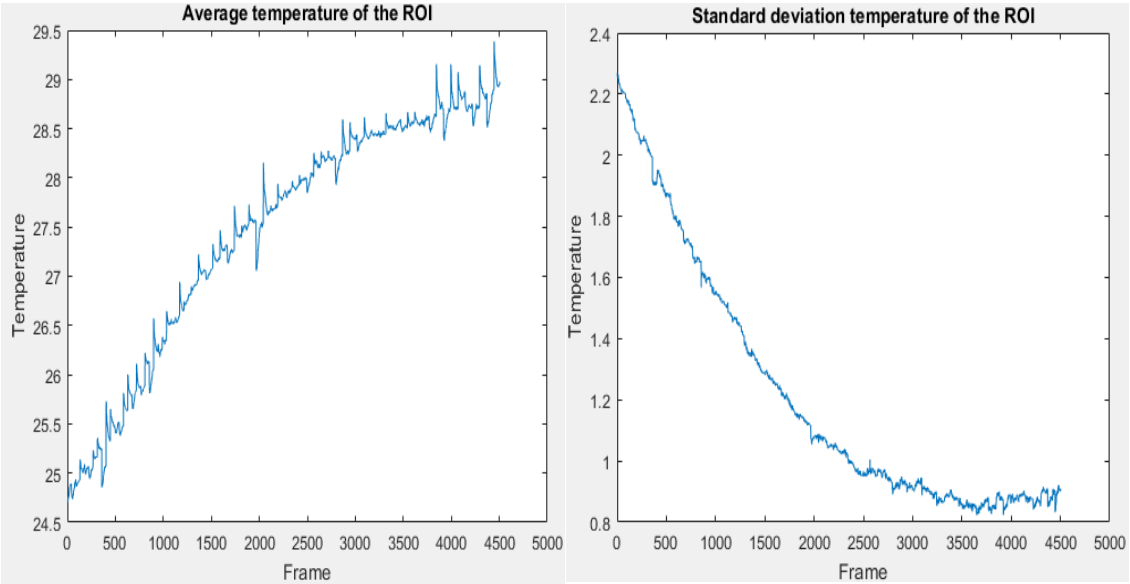

Figure 25. Average temperature and standard deviation of the ROI observed from the subject 1.

In Figure 25, we noticed that the average of minimum temperature of the ROI is 24.57°C and the average of maximum temperature of the ROI obtained is 29.4 °C, this data corresponds to the range of frame [0, 4500] for x coordinate. The minimum of standard deviation temperature of the ROI is 0.81°C and the maximum of standard deviation temperature of the ROI is 2.29 °C, this data corresponds to the range of frame [0, 4500] for x coordinate. Thus, the frequency of the curve for average temperature is fast, the spike of the curve is little fast compared to Figure 27.

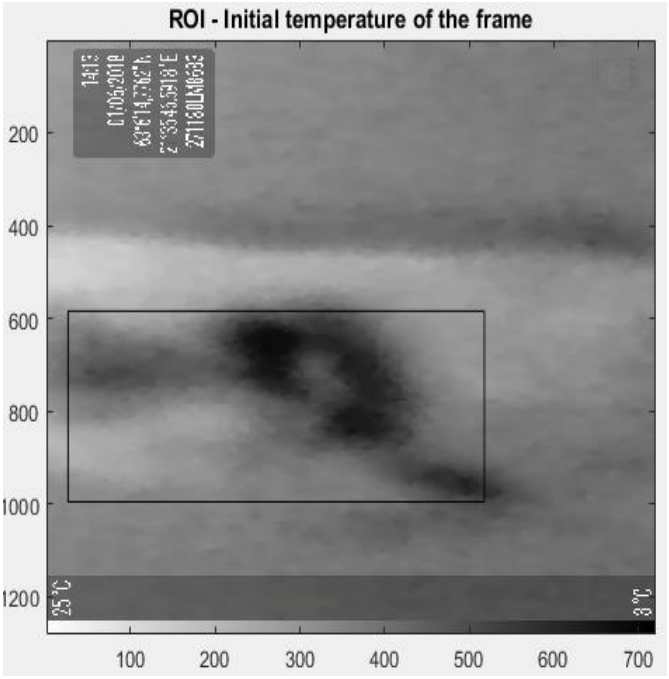

Figure 26. Initial temperature on the frame of the ROI observed on the subject 2 after applied thermoregulation dynamic.

In the figure 26, the ROI is located in the portion of ice disturbance between range of [20, 540] for y coordinate and range of [580, 1000] for x coordinate.

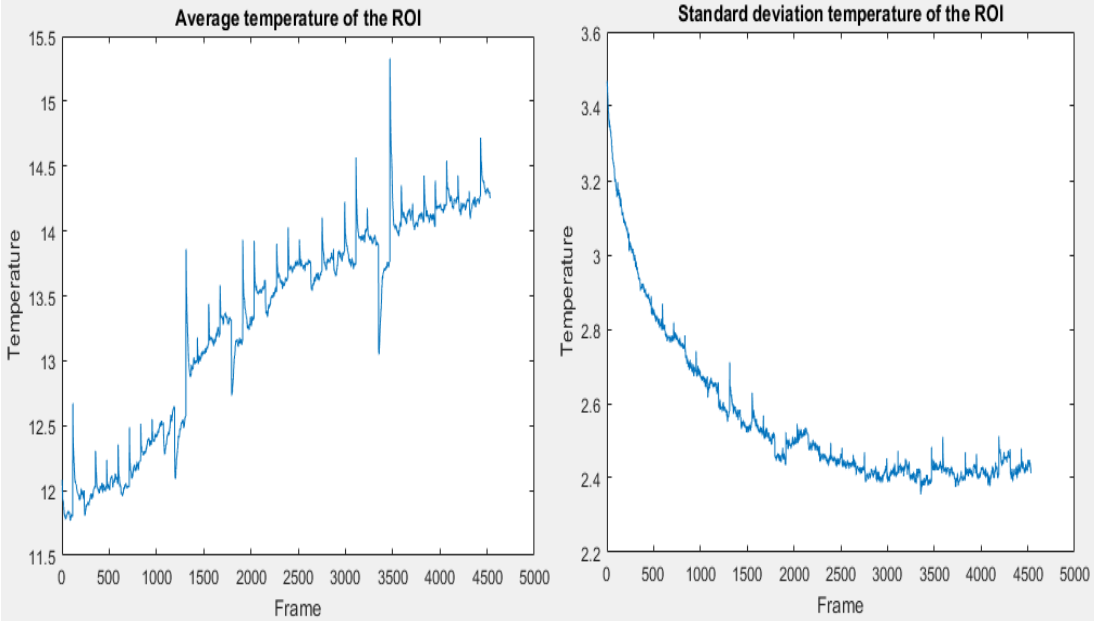

Figure 27. Average temperature and standard deviation of the ROI observed from the subject 2.

In Figure 27, we noticed that the average of minimum temperature of the ROI is 11.57°C and the average of maximum temperature of the ROI obtained is 14.4 °C, this data corresponds to the range of frame [0, 4500] for x coordinate. The minimum of standard deviation temperature of the ROI is 2.43 °C and the maximum of standard deviation temperature of the ROI is 3.46 °C, this data corresponds to the range of frame [0, 4500] for x coordinate. Thus, the frequency of the curve for average temperature is slow according to the minimum temperature T° = 3 °C observed from Figure 29, the spike of the curve is slow compared to Figure 25.

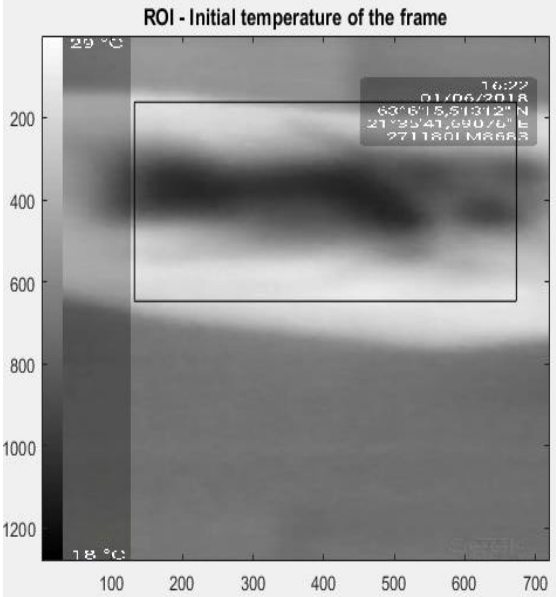

Figure 28. Initial temperature on the frame of the ROI observed on the subject 3 after applied thermoregulation dynamic.

In the figure 28, the ROI is located in the portion of ice disturbance between range of [160, 640] for y coordinate and range of [140, 670] for x coordinate.

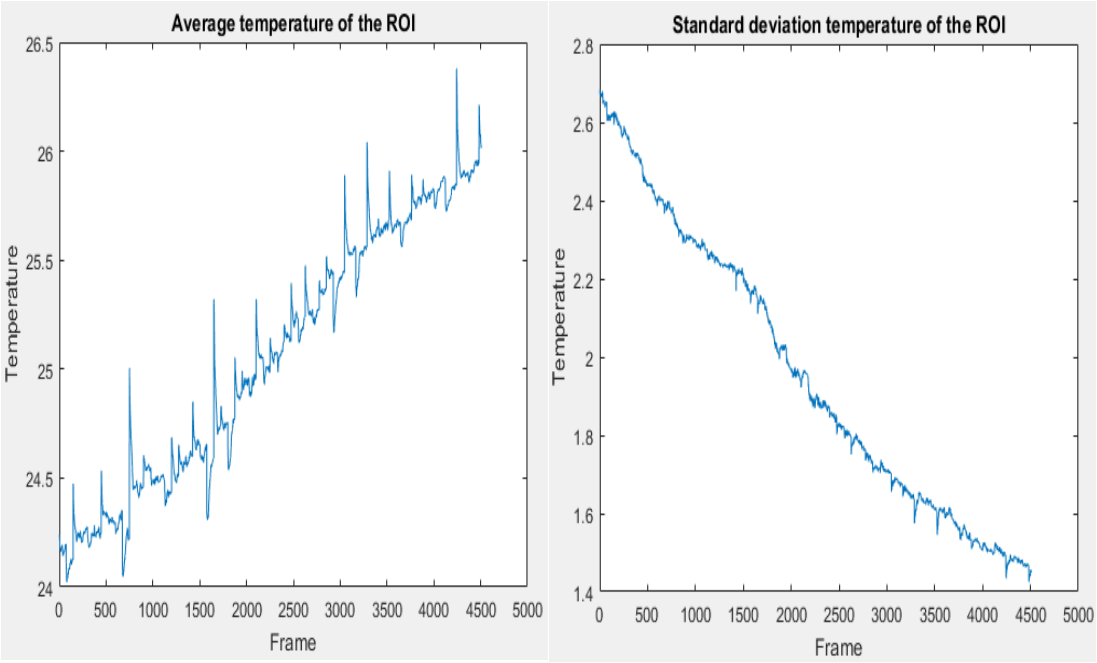

Figure 29. Average temperature and standard deviation of the ROI observed from the subject 3.

In Figure 29, we noticed that the average of minimum temperature of the ROI is 24.2 °C and the average of maximum temperature of the ROI obtained is 26.4 °C, this data corresponds to the range of frame [0, 4500] for x coordinate. The minimum of standard deviation temperature of the ROI is 1.41 °C and the maximum of standard deviation temperature of the ROI is 2.69 °C, this data corresponds to the range of frame [0, 4500] for x coordinate. Thus, the frequency of the curve for average temperature is fast and the spike of the curve is fast compared to Figure 27.

T = 0, after using ice (Time instant) at the beginning.

Table 1. Temperature variations of the 3 subjects observed in the experimental test.

Subject	**T_{ROI} (°C)**		**$\langle T \rangle_{ROI}$ (°C)**	**$\sigma(T_{ROI})$ (°C)**
	Tmin	**Tmax**		
Suject 1	20	32	24.7	2.25
Subject 2	3	25	12.1	3.47
Subject 3	18	29	24.1	2.67

Where Tmin, Tmax and T_{ROI} denoted minimum temperature, maximum temperature and temperature of the ROI respectively, $\langle T \rangle_{ROI}$ denoted average temperature of the ROI and $\sigma(T_{ROI})$ denoted standard deviation temperature of the ROI.

Let consider the data from Table 1, we noticed that the average of minimum temperature of the ROI is 13.6 °C, the average of maximum temperature of the ROI obtained is 28.6 °C, the mean of temperature of the ROI is 20.3 and the standard deviation of the

ROI is 2.79 °C. Thus, the rate of the curve is slow, the spike of the curve is little fast compared to that observe in Figure 27, the mean scaled score is 20.1, and the standard deviation scaled absolute is 2.78 °C.

Following the results of standard deviations obtained in different graphs from the 3 subjects shown that, the same data may be repeated of the test from second subject foot. Because, the body temperature is regulated in all body parts. Thus, the standard deviation could be totally different with the new subjects submitted at the same experiment.

Therefore, the corresponding images are presented in the spectral imaging analysis, when we applied the standardized protocol with visual analysis, textures, colorbar aspect level, variability, shapes, orientations between both subject's feet, and extraction images variable from channels.

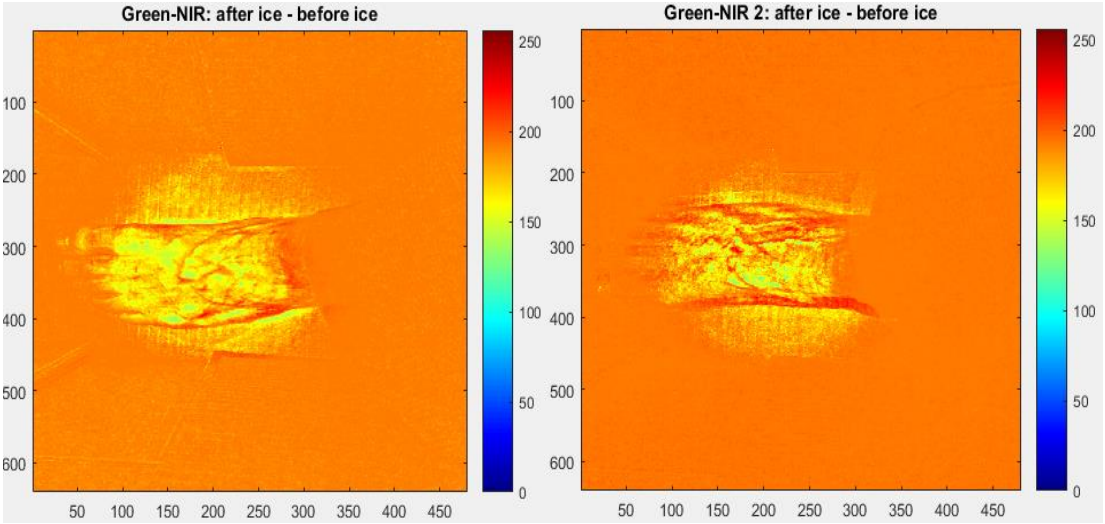

Figure 30. Spectral imaging analysis for Green-NIR channels on the subject's feet. Difference between before and after applied thermoregulation dynamic on the ROI.

We observed the higher perspective and temporal dynamic were more visible from the ROI for the right foot compared to the left foot, and the texture changed for both feet according to the colorbar level around 175.

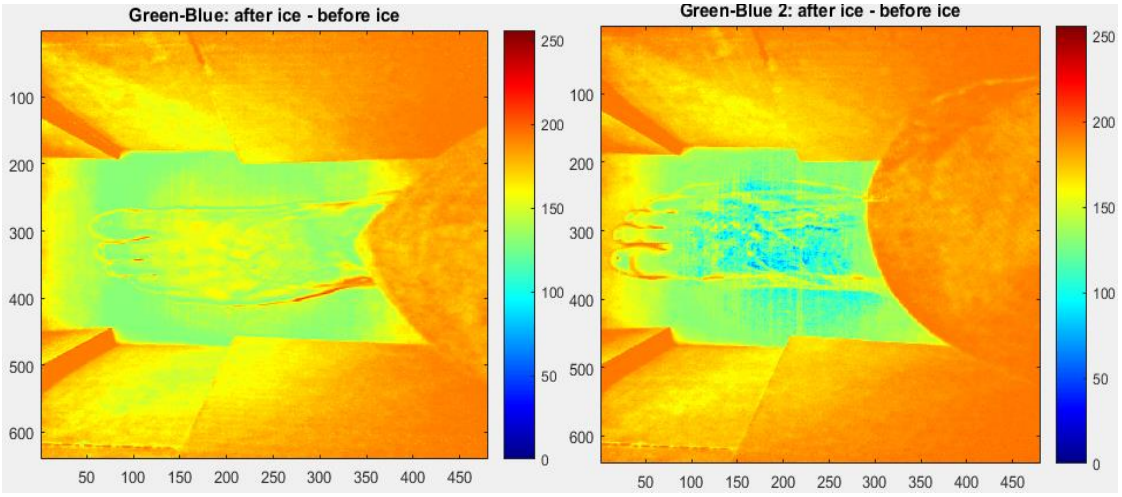

Figure 31. Spectral imaging analysis for Green-Blue channels on the subject's feet. Difference between before and after applied thermoregulation dynamic.

The higher perspective, temporal dynamic and spatial variation were observed from the ROI for the right foot compared to the left foot, and the texture also changed on the subject's right foot according to the colorbar level around 175.

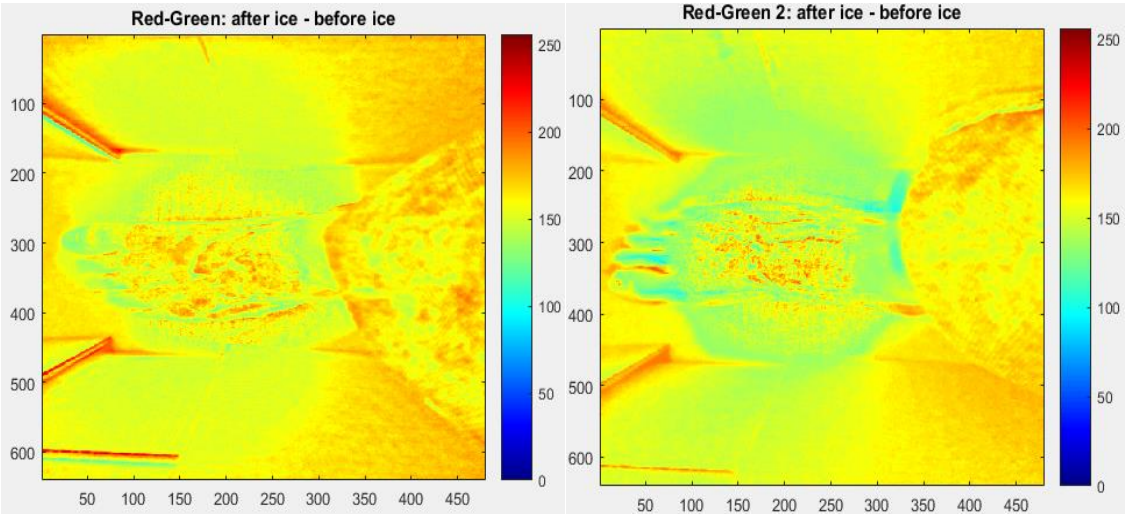

Figure 32. Spectral imaging analysis for Red-Green channels on the subject's feet before applied thermoregulation dynamic.

The temporal dynamic, spatial variation and higher perspective were observed on the ROI from the subject's left foot, but the texture is little lower for colorbar level. No real change was observed in Figure 32.

The image fusion test have improved enough in way that we observed the image fusion foot despite the difference of visual observation relative of texture, estimation of the spatial variations and temporal dynamics between spectral images on the ROI.

Some images obtained from this test were totally dark in such a way, we could not observe any change in the ROI according the increased texture and the shape derivation appears during the final image fusion.

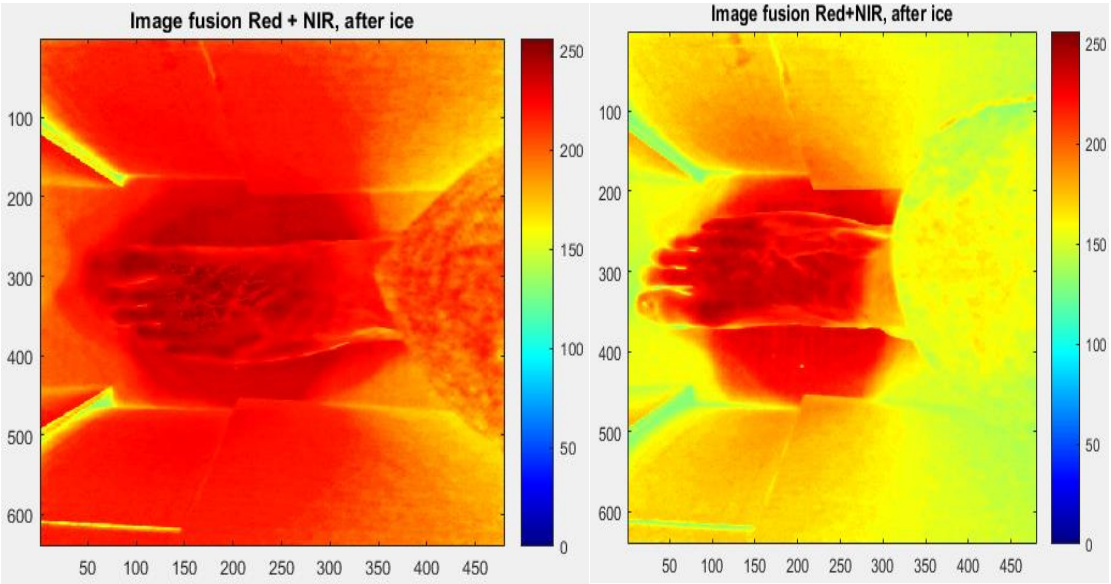

Figure 33. Fusion image of Red-NIR channels and thermal image on the subject's feet after applied thermoregulation dynamic.

In Figure 33, It implies that the concentration of blood circulation appeared for the large texture in the ROI of the left foot i.e. the spatial variations are stronger. In contract, image fusion for the right foot does not show significant texture, and saturated values have be observed in the ROI, with a perfect estimation of spatial variations, higher perspective for blood circulation and fluid hemoglobin observed from both feet.

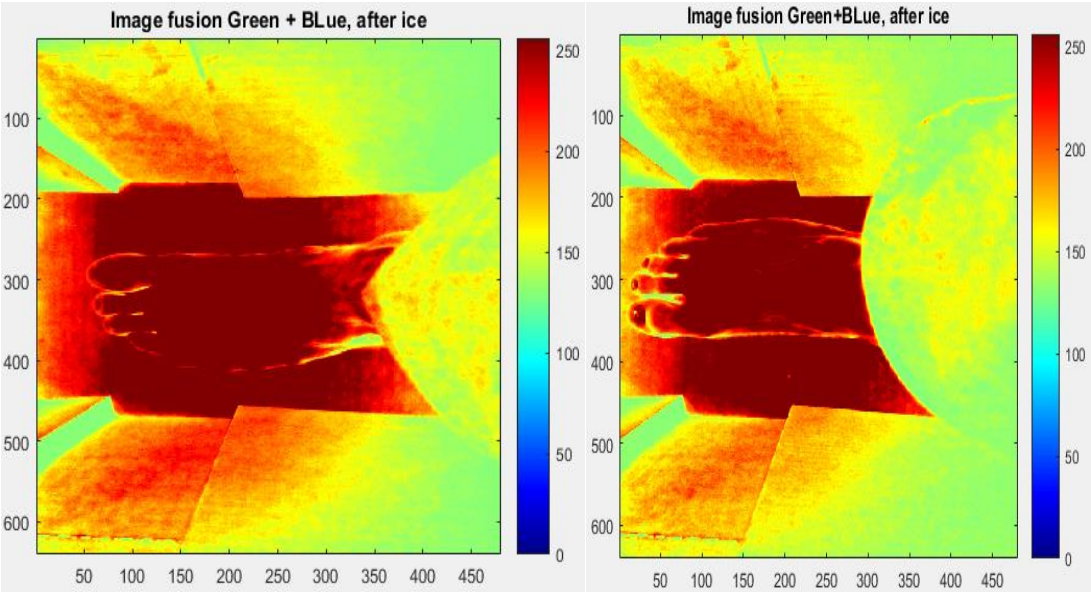

Figure 34. Fusion image of Green-Blue channels and thermal image on the subject's feet after applied thermoregulation dynamic.

The results of our study show that thermal imaging provides logical analysis based on maximum and minimum temperature, average temperature, and standard deviation temperature of the obtained ROI. The body temperature data can provide information to observe the normal regulation of blood circulation. The diabetic foot can be located from different indications such that the peripheral circulation region sweating dysfunction and the thermoregulatory disturbance. But, this normal regulation may be also affected by humidity and temperature environment. In addition, experimental procedure and image analysis methods based on thermal images, comparisons of spectral images and curves (Figures 25 and 27) done are correlated to the prediction indices earlier observed in sections 3.4.2, 3.4.3 and 4.3.1.

In order to illustrate Figures 31, 32, 33 and 34 following the theory explained in sections 3.2 and 3.3 applied to colours, wavelength, frequencies and energy of the visible light spectrum in correlation with the principles of Plank's law and Wien's displacement law. We compared theory mentioned that spectral imaging analysis done using images channels radiation Green-Blue emitted are smaller than Red-Green and images channels radiation Red-NIR emitted are higher than Green-Blue. In Figures 5 and 6, we realized from different colour scales that this concept acted on the emissivity, intensity of energy

and frequency values of different image channels used, which affect the luminance and chrominance described in the images perception from grayscale spectrum absorption.

Hence, RGB+NIR colour model is an identification of the diabetics using thermal and spectral foot images. Thus, the detection of diabetics can be detected based on the skin colours at the earlier stage. Spectral imaging method is used for the measurement of oxygen saturation and total hemoglobin concentration maps of the feet of both diabetic and non-diabetic subjects from skin spectra from the quality of NIR spectra characterized by image fusion analysis. Thermal imaging is a method used to monitor skin temperature in the ROI, which assess the efficacy of treatment used by the diabetic subject to improve the perfusion to the affected limb.

Finally, the segmentation map of non-diabetic foot image is the number of texture colour patched in spectral images during the diabetic test. This method is Hager-Zhang algorithm developed with nonlinear models. Thus, according to spectral and thermal images observed during the implementation test and obtained results, we can easily mention that the subjects are non-diabetic subjects. In brief, the probabilities appeared in the table shows that the subjects are healthy.

6 CONCLUSIONS AND FUTURE WORK

In this thesis, a model system was expanded to give thermal and spectral images and body temperature values without being comfy and non-confined for experiments done. Smartphones were used to take both thermal and spectral images, the last-mentioned with the assistance of monochromatic LEDs provide to enhance image qualities obtained. Our study was focused mainly on thermal image analysis as an effective tool used in risk detection or visual- percept of the diabetic foot. This indicator is a confined process that reports temperature variations data from the temperature of the subjects 'foot and temporal dynamics of surface (ROI) used for experiments. Hence, our study reveals the necessity of thermal image procedure based on temperature texture analysis of the human skin conditioned by its environment. The objective is also emphasized on the spectral or hyperspectral imaging as temporal dynamics proposed, which performs a digital image or video of the foot with different colours channel for enhancement each pixel quality contained in the frame, in order to simplify different temperatures analysis of images used in the frame during our experiments.

In addition, the target of present study was to consider the correlation among DRS evaluation and tissue oxygenation process during an image merge operation. Nevertheless, this theory explained in sections 3.6, 4.2.1 and 4.3.1 is applied here from the image generated by thermal infrared radiation is referred as a thermogram. Hence, inspected ROI for the test person feet test occurs to the effect of body infrared radiation observed in Figures 34 and 34 of experiments. Although, the NIR located wave infrared region occupies wavelengths used in the subjects' foot, which shows the effect of radiation observed in the ROI during the experiments.

The approach of the proposed methodology was tested with three healthy test subjects' relative of the thermoregulation dynamics by using thermal images and spectral imaging in different patients and to obtain the accurate data for average and standard deviation temperature, in such way to notice about blood circulation based on oxiometry which ameliorates to a prompt diagnostic of diabetic foot risks. The spectral imaging analysis

and the results obtained during these experiments entice our attention to Hager-Zhang algorithm based on the image segmentation, which used from the number of monochromatic colours repaired on the subject's foot image to diagnose diabetes disease.

In contrast, the results observed in Figures 30, 31, 32, 33 and 34 could be totally different in case the subjects come from several continents with different life standard, or the test patients have been realized in different areas in the world. Therefore, those variations elements can be linked to human morphology and different body radiation levels (blackbody, graybody and greybody). To illustrate this idea, human skin has an accurate emissivity coefficient in the entire spectral range and human skin is also a temperature detector relied upon morphological variables of the human body. Thus, the human skin consists of isotherms with high temperature variations that can be influenced by endogenous and exogenous factors. Therefore, skin temperature can be examined from thermal emission using thermal imaging as a non-invasive and non-contact technique. In this situation, we can also be uncertain of reliability of tools used in testing experiments; as such experiments require the collaboration of a more specialized medical unit, in order to avoid diagnostic errors to the nearest millimetre.

In the future, there will be two main development points for the system: first, to automate the measurement system, so that the patient could use it alone. Second, it is needed to improve the spectroscopic measurement system and analysis in order to have a better view of the blood circulation state.

REFERENCES

Abdel-Aziz Y.I. & Karara H.M. (1971). Direct linear transformation into object space coordinates in close-range photogrammetry, *Symposium on Close-Range Photogrammetry*; pp.1-18.

Acha B., Serrano C., Acha J. I. & Roa L. M. (2005). Segmentation and classification of burn images by colour and texture information, *Journal of Biomedical Optics*; 10(3).

Ammer K. (2008). The Glamorgan protocol for recording and evaluation of thermal images of the human body. *Thermology International*, pp.18:125–129.

Apelqvist J. (2008). The foot in perspective. *Diabetes Metab Res Rev*; 24 (Suppl. 1): S110 - 5.

Armstrong D.G., et al. (1997). Infrared dermal thermometry for the high-risk diabetic foot, *Physical Therapy*, 77(2): pp. 169.

Armstrong D.G., Lavery L., Wunderlich R. & Boulton A. (2003). Skin temperatures as a one-time screening tool do not predict future diabetic foot complications, *J Am Podiatr Med Assoc*. 93:443-7.

Bagavathiappan S., et al., (2009). Infrared thermal imaging for detection of peripheral vascular disorders. *Journal of Medical Physics*, 34(1).

Bakker K., Apelqvist J. & Schaper N.C. (2011). Practical guidelines on the management and prevention of the diabetic foot. *International Working Group on the DiabeticFoot Editorial Board IWGDF and Diabetes Metab Res Rev 2012*; 28 (Suppl 1): 225–231.

Bharara M., Cobb J.E. & Claremont D.J. (2006). Thermography and thermometry in the assessment of diabetic neuropathic foot: a case for furthering the role of thermal techniques. *International Journal of Lower Extremity Wounds*; 5(4): 250–260.

Borgefors G. (1984). Distance Transformations in Arbitrary Dimensions. *Proceedings of Computer Vision, Graph Image Processing*, 27, pp. 321-345.

Bykowski J., Kollias N. & LaMuraglia G. (2004). Evaluation of peripheral arterial occlusive disease and postsurgical viability using reflectance spectroscopy of skin. *Microvascular Research*, 67 (2): pp. 152-158.

Chan A.W., MacFarlane I.A. & Bowsher D.R. (1991). Contact thermography of painful diabetic neuropathic foot, *Diabetes Care*; 14:918e22.

Cielo P. & Vaudreuil G. (1992). Infrared temperature sensors for control of the surface melting process on superconducting ceramics, *in Proceedings of the LAMP '92, Nagoaka*; pp. 421-426.

Delbridge L., Ctercteko G., Fowler C., Reeve T.S. & Le Quesne L.P. (1985). The aetiology of diabetic neuropathic ulceration of the foot. *Br J Surg*.; 72(1):1-6.

Dreniak E.L. & Boreman G.D. (1996). Infrared detectors and systems, *Wiley-Interscience publication, John Wiley & Sons, Inc*, New York.

Duarte A., Carrão L., Espanha M., Viana T., Freitas D., Bártolo P., Faria P., Almeida H. (2014). Segmentation algorithms for thermal images. *Procedia Technology;* 16, 1560-1569.

Durduran T, Yu G, Burnett M.G, Detre J.A, Greenberg J.H, Wang J, Zhou C & Yodh A.G. (2004). Diffuse optical measurement of blood flow, blood oxygenation, and me-

tabolism in a human brain during sensorimotor cortex activation. *Optics Letters*; 29(15): pp. 1766-1768.

Faig W. (1975). Calibration of close-range photogrammetric systems: Mathematical formulation, *Photogrammetric Eng. Remote Sensing*, vol. 41, no. 12, pp. 1479-1486.

Fauci M.A., Breiter R., Cabanski W., Fick W., Koch R., Ziegler J. & Gunapala S.D. (2001). Medical infrared imaging–differentiating facts from fiction and the impact of high precision quantum well infrared photodetector camera systems, and other factors, in its reemergence. *Infrared Physics and Technology*, 42(3-5): pp. 337-344.

Finlay J.C. & Foster T.H. (2004). Hemoglobin oxygen saturations in phantoms and in vivo from measurements of steady-state diffuse reflectance at a single, short source-detector separation, Med. Phys.; 31(7), 1949–1959.

Flynn M. & Tooke J. (1995). Diabetic neuropathy and the microcirculation. *Diabetic Medicine*; 12:298-301.

Gejgus P., Placek J. & Sperka M. (2004). Skin colour segmentation method based on mixture of Gaussians and its application in learning system for finger alphabet, *International Conference on Computer Systems and Technologies*.

Gershater M.A., Löndahl M., Nyberg P., Larsson J., Thörne J., Eneroth M. & Apelqvist J. (2009). Complexity of factors related to outcome of neuropathic and neuroischaemic/ischaemic diabetic foot ulcers: a cohort study. *Diabetologia*; 52(3): 398-407.

Gowen A., O'Donnell C.P, Cullen P.J., Downey G. & Frías J.M. (2007). Hyperspectral imaging–an emerging process analytical tool for food quality and safety control. *Trends in Food Science & Technology*; 18 (12): p. 590-598.

Huang Y., Yan Y. & Riley G. (2000). Vision-based Measurement of Temperature Distribution in a 500-kW Model Furnace Using the Two-colour Method, *Measurement 28*, pp. 175-183.

Hui L., Peijun D., Weichang Z., Lianpeng Z. & Huasheng S. (2010). Image Registration Based on Corner Detection and Affine Transformation, In the *Proceedings of 3rd International Congress on Image and Signal Processing*.

Jianbo G., Jun Z., Matthew G., Fleming, Ilya P. & Cognetta A.B. (1998). Segmentation of dermatoscopic Images by Stabilized Inverse Diffusion Equations, *IEEE Computer Society*.

Johnston B.G (1994). Three-Dimensional Multispectral Stochastic Image Segmentation. Memorial University of Newfoundland, Cabot Institute of Technology.

Jones M.J. & Rehg J.M. (1999). "*Statistical color models with application to skin detection*". In Proceedings of the CVPR; vol. 1, 274-280.

Kalish J. & Hamdan A. (2010). Management of diabetic foot problems. *J Vasc Surg*; 51 (2): 476-86.

Khaodhiar L., Dinh T., Schomacker K.T., Panasyuk S.V., Freeman J.E., Lew R., Vo T., Panasyuk A.A., Lima C., Giurini J.M., Lyons T.E. & Veves A. (2007).The use of medical hyperspectral technology to evaluate microcirculatory changes in diabetic foot ulcers and to predict clinical outcomes. *Diabetes care*; 30(4): p. 903-910.

Kocsis L., Herman P. & Eke A. (2006). The modified Beer-Lambert law revisited, *Physics in Medicine and Biology*; 51(5), 91-98.

Kong S.G, Chen Y.R, Kim I & Kim M.S. (2004). Analysis of hyperspectral fluorescence images for poultry skin tumor inspection. *Applied optics*, 43 (4): p. 824-833.

Lavery L.A., Higgins K.R., Lanctot D.R., Constantinides G.P., Zamorano R.G., Armstrong D.G., Athanasiou K.A. & Agrawal C.M. (2004). Home monitoring of foot skin temperatures to prevent ulceration. *Diabetes Car*e; 27, 2642–2647.

Lambert J. (1760). Photometrie. Photometria sive de ensura et gradibus luminis, colorum et umbrae. *1st edition Augsburg: Eberhardt Klett*; p.391.

Lepäntalo M., Apelqvist J., Setacci C., Ricco J.B., de Donato G., Becker F., Robert-Ebadi H., Cao P., Eckstein H.H., De Rango P., Diehm N,. Schmidli J., Teraa M., Moll F.L., Dick F., Davies A.H. (2011). Chapter V: Diabetic Foot, *European Journal of Vascular and Endovascular Surgery*; 42(S2), S60–S74

Mekhontsev S.N., Prokhorov A.V. & Hanssen L.M. (2010). Experimental characterization of blackbody radiation sources. In: Zhang ZM, Tsai BK, Machin G, editors. *Radiometric Temperature Measurements*. II. Applications. Elsevier: pp. 57–136.

Meola C. (2012). Origin and Theory of Infrared Thermography. In *Infrared Thermography: Recent Advances and Future Trends; Meola, C., Ed.; Bentham Science*: New York, NY, USA.

Merla A. & Romani G. L. (2005). Functional infrared imaging in clinical applications. In: *The Biomedical Engineering Handbook,* edited by J. D. Bronzino. New York, NY: *CRC Press;* 32.1–32.13.

Michalski L., Eckersdorf K. & McGhee J. (1991). *Temperature Measurement*, J. Wiley, New Sussex, UK.

Mitchell H.B. (2010). Image Fusion: Theories, Techniques and Applications. Springer.

More J.J. (1978). The Levenberg-Marquardt algorithm: Implementation and theory. *Lecture Notes in Num. Appl. Anal, Notes in Math*. pp. 630, 105–116

Mourant J.R. & Bigio I.J. (2003). Elastic-scattering spectroscopy and diffuse reflectance, in *Biomedical Photonics Handbook, T. Vo-Dinh, Editor. CRC Press*.

Murff R.T., Armstrong D.G., Lanctot D., Lavery L.A. & Athanasiou K.A. (1998). How effective is manual palpation in detecting subtle temperature differences? *Clin. Podiatr. Med.Surg.* 15(1), 151–154.

Nagase T., Sanada H., Takehara K., Oe M., Iizaka S., Ohashi Y., Oba M., KadowakiT., Nakagami G. (2011). Variations of plantar thermographic patterns in normal controls andnon-ulcer diabetic patients: Novel classification using angiosome concept. *Journal of Plastic, Reconstructive & Aesthetic Surgery*; 64, 860 – 866.

Nouvong A., Hoogwerf B., Mohler E., Davis B., Tajaddini A. & Medenilla E. (2009). Evaluation of diabetic foot ulcer healing with hyperspectral imaging of oxyhemoglobin and deoxyhemoglobin, *Diabetes Care*; 32(11), 2056.2061.

Palumbo P.J. & Melton L.J.III. (1995). Peripheral vascular disease and diabetes. *Diabetes in America;* 2: 401-8.

Papazoglou E.S., Weingarten M.S., Zubkov L., Neidrauer M., Zhu L., Tyagi S. & Pourrezaei K. (2008). Changes in optical properties of tissue during acute wound healing in an animal model. *Journal of Biomedical Optics*. 13: p. 044005.

Poynton C.A. (1995). Frequently asked questions about colour. Available from: *ftp://www.inforamp.net/pub/users/poynton/doc/colour/ColorFAQ.ps.gz*.

Prahl S. (1998).Optical absorption of hemoglobin. *Oregon Medical Laser Center,* USA,

Rayman G, Williams S, Spencer P, Smaje L, Wise P & Tooke J. (1986). Impaired microvascular hyperaemic response to minor skin trauma in type 1 diabetes. *Br Med J*; 292:1295-8.

Reiber G.E & Ledoux W.R. (2003). Epidemiology of diabetic foot ulcers and amputations: Evidence for prevention. In: *Williams R, Herman W, Kinmonth AL, Wareham NJ, editors.* The evidence base for diabetes care. Chichester*; Hoboken (NJ): John Wiley & Sons,* Ltd; pp: 641–665.

Renier E., Meriaudeau F., Suzeau P. & Truchetet F. (1996). CCD Temperature Imaging: Applications in Steel Industry, Industrial Electronics, Control, and Instrumentation, *Proceedings of the IEEE IECON 22nd International Conference* on, Vol: 2, pp. 1295–1300.

Richtlinie VDE. (1995). Technische Temperaturmessungen-Strahlungsthermometrie. *VDI* 3511; pp 4.

Ring E.F.J. & Ammer K. (2000). Quantitative thermal imaging. *Clin Phys Physiol Meas.*; 11(SA), 87-95.

Roback K. (2010). An overview of temperature monitoring devices for early detection of diabetic foot disorders. *Expert Rev. Med. Devices*; 7(5), 711–718.

Roback K., Johansson M. & Starkhammar A. (2009). Feasibility of a thermographic method for early detection of foot disorders in diabetes, *Diabetes Technology & Therapeutics*; 11, 663–337.

Round A.J., Duller A.W.G. & Fish P.J. (1997). Colour Segmentation For Lesion Classification, *IEEE/EMBS* Chicago, IL. USA

Steketee J. (1973). Spectral emissivity of skin and pericardium. *Phys. Med. Biol.*; 18, 686–694

Stess R.M., Sisney P.C., Moss K.M., Graf P.M., Louie K.S., Gooding GA, et al. (1986). Use of liquid crystal thermography in the evaluation of the diabetic foot, *Diabetes Care*; 9:267-72.

Suresh A.B.S. & Sujatha N. (2011). Quantification of tissue oxygenation levels using diffuse reflectance spectroscopy. *Tenth International Conference on Fiber Optics and Photonics, 817308, Proc. SPIE 8173, Photonics*.

Tomaz F., Candeias T., Shahbazkia H. (2016). Fast and accurate skin segmentation in color Images, *Proceedings of the First Canadian Conference on Computer and Robot Vision*; (CRV'04).

Tsai R.Y. (1987). A versatile camera calibration technique for high accuracy 3-D machine vision metrology using off-the-shelf TV cameras and lenses, *IEEE J. Robotics Automat*. Vol. RA-3, No. 4, pp. 323-344.

Usamentiaga R., Venegas P., Guerediaga J., Vega L., Molleda J. & Bulnes F.G. (2014). Infrared thermography for temperature measurement and non-destructive testing. *Sensors 14*.

Vilcahuaman L. (2013) Early Diagnosis of Diabetic Foot Using Thermal Images, *Université D'Orléans, France*.

Vinik A.I., Maser R.E., Mitchell B.D. & Freeman R. (2003). Diabetic autonomic neuropathy. *Diabetes Care*; 26:1553–1579.

Wang H., Peng J. & Wu W. (2002). Fusion algorithm for multisensory images based on discrete multiwavelet transform, Vision, *Proceedings of the IEEE*; Image and Signal Processing Vol.149, no.5.

Weingarten M.S., Papazoglou E.S., Zubkov L., Zhu L., Neidrauer M., Savir G., Peace K., Newby J.G. & Pourrezaei K. (2008). Correlation of near infrared absorption and diffuse reflectance spectroscopy scattering with tissue neovascularization and collagen concentration in a diabetic rat wound healing model. *Wound Repair and Regeneration*, 16 (2): p. 234-242.

Weingarten M.S., Papazoglou E., Zubkov L., Zhu L., Vorona G. & Walchack A. (2006). Measurement of optical properties to quantify healing of chronic diabetic wounds. *Wound Repair and Regeneration*, 14(3): p. 364-370.

Zhang J.Y., Chen Y. & Huang X.X. (2009). IR Thermal Image Segmentation Based on Enhanced Genetic Algorithms and Two-Dimensional Classes Square Error. *Second International Conference on Information and Computing Science.*

Zijlstra,W., Buursma A., & Meeuwsen-Van Der Roest W. (1991). Absorption spectra of human fetal and adult oxyhemoglobin, de-oxyhemoglobin, carboxyhemoglobin, and methemoglobin. *Clinical Chemistry*; 37(9): p. 1633.

Zuzak K.J., Schaeberle M.D., Lewis E.N. & Levin I.W. (2002). Visible reflectance hyperspectral imaging: characterization of a non-invasive, in-vivo system for determining tissue perfusion, *Anal. Chem.*; 74(9), 2021-202.